Microstructured Tungsten Thermophotovoltaic Selective Emitters

by

Natalija (Zorana) Jovanović

B.S., University of Illinois at Chicago (2002)

S.M., Massachusetts Institute of Technology (2005)

Submitted to the Department of Electrical Engineering and Computer Science
in partial fulfillment of the requirements for the degree of

Doctor of Philosophy
[Sc. D.]
at the

MASSACHUSETTS INSTITUTE OF TECHNOLOGY

June 2008

Author_____
Department of Electrical Engineering and Computer Science
June 2008

Certified by_____
John G. Kassakian
Professor of Electrical Engineering and Computer Science
Thesis Supervisor

Certified by_____
Leslie A. Kolodziejski
Professor of Electrical Engineering and Computer Science
Thesis Supervisor

Accepted by_____
Prof. Terry P. Orlando
Chair, Department Committee on Graduate Students

Microstructured Tungsten Thermophotovoltaic Selective Emitters

by

Natalija (Zorana) Jovanović

Submitted to the Department of Electrical Engineering and Computer Science
on June 2008, in partial fulfillment of the
requirements for the degree of
Doctor of Philosophy

Abstract

This research investigates the fabrication, modeling, characterization, and application of tungsten two-dimensional (2D) photonic crystal (PhC) structures as selective emitters and means of achieving higher efficiencies in thermophotovoltaic (TPV) energy conversion systems. Important aspects of the fabrication process are researched, developed, and rigorously characterized, focusing on dimensional reliability, precision, and repeatability of the processes. A major contribution in the form of tungsten reactive ion etch (RIE) characterization is provided with detailed parameters and second-order influences on etch rate, smoothness, and mask erosion. Optical characterization of our prototypes is found to be in excellent agreement with simulation, and has provided an experimental confirmation of selective emitter performance. We show that selective emitters can substantially increase spectral efficiency, providing as much as three times the radiative power density of planar tungsten. We include the first measurement of 96% combined efficiency of a selective emitter and a dielectric stack mirror for TPV system applications.

Thesis Supervisor: John G. Kassakian
Title: Professor of Electrical Engineering and Computer Science

Thesis Supervisor: Leslie A. Kolodziejski
Title: Professor of Electrical Engineering and Computer Science

Acknowledgements

During the course of my education at the Massachusetts Institute of Technology I have been privileged to work with many truly exceptional individuals. I am deeply grateful to Prof. John Kassakian for the opportunities he has provided in my education. Prof. Kassakian's instruction and mentorship have shaped my development both as a scientist and as a person. Prof. Leslie Kolodziejski has artfully maintained impressive balance between stimulating critical thought and heartfelt encouragement throughout the project. I would like to thank Prof. David Perreault for his continuous dedication to technical quality of this work. Dr. Ivan Čelanović's enthusiasm and allegiance to the MIT TPV project have made it possible for me to last through some of the most challenging times during this endeavor.

The sponsorship for my education at MIT and for this research project has been provided by the MIT Presidential Fellowship, MIT/Industry Consortium on Advanced Automotive Electrical/Electronic Components and Systems, the Landsman Charitable Trust, and the Toyota Motor Corporation. I am particularly grateful to Mr. Akinori Sato and Dr. Tomonori Nagashima of Toyota for their instruction, dedication to quality, and patience as we managed our collaboration.

This thesis would not have been possible without the Laboratory for Electromagnetic and Electronic Systems and the many wonderful students, staff and faculty who comprise it. I'd like to especially thank Dr. Thomas Keim for his insight on TPV issues, and Gary DesGroseilliers for assuring that the project was adequately supported. Working alongside dedicated colleagues has been a real pleasure: I will keep fond memories of numerous technical and non-technical conversations with Frank O'Sullivan, Karin Strasswimer, Yihui Qiu, Laura Zager, Alejandro Dominguez-Garcia, Vivian Mizuno, and many others with whom I had the pleasure to share some of my LEES years.

The microfabrication section of this research has been carried out at the MIT NanoStructures Laboratory. I am indebted to Prof. Henry Smith and Prof. Karl Berggren for accepting me as one of the NSL collaborators. Drs. Michael Walsh, Gale Petrich (of RLE), Thomas O'Reilly, Tim Savas, and Euclid Moon were my instructors as I was learning the ropes of NSL. It is widely known that none of the research in NSL would be possible without the technical know-how and perseverance of James Daley. Candid conversations with many fellow NSL students made the long fab hours pass faster. The collection of emission spectra results was enabled by Elizabeth Shaw and Tim McClure of the MIT Center for

Materials Science and Engineering, and LEES undergraduate researchers Stephen Zhou, David Jenicek, Adrian Yeng, Sabrina Neuman, Francisco Zenteno, and Kang Gao.

The last six years have been filled with many joys and challenges. Despite intercontinental distance, my parents Zoran and Zorica stood by me every step of the way. During the most difficult times I knew I could count on my partner Mitchell Peabody for strength and encouragement. I hope that future joys will balance out the difficulties we've faced so far. Bursts of inspiration and optimism came from the loving heart of Debb Hodges-Pabon. Any long journey is always made better by company, and I am grateful to Karen, Nina, Fadi, Lina, Ajit, Song-Hee, Vivian, all of ghetto-retto, Rainbow Coffeehouse, MOST, Sidney-Pacific and many others for creating some fantastic memories along the PhD way.

Contents

1 Introduction **12**

1.1 Thermophotovoltaic Systems 12

1.1.1 Emitter 13

1.1.2 PV Diode 14

1.1.3 System Efficiency 15

1.2 Spectral Control Via Selective Emitters 16

1.2.1 Selectivity Due to Material Properties 17

1.2.2 Selectivity Due to Physical Structuring 19

1.2.3 Synergy of Material Properties and Physical Structuring 20

1.3 Contributions and Structure 22

2 Results **23**

2.1 Theory 23

2.2 Simulations 25

2.3 Dimensional Characterization 26

2.4 Room-Temperature Spectral Characterization 27

2.4.1 Flat Tungsten 29

2.4.2 Selective Emitter Prototypes 32

2.4.3 Spectral Efficiency 37

2.5 High-Temperature Spectral Characterization 41

2.6 Summary 47

3 Fabrication Methods **49**

3.1 Process Flow 49

3.1.1 A Note on Calibration Procedures 50

3.2 Lithography 51
3.2.1 Hexagonal Pattern Lithography 58
3.3 Etching 60
3.3.1 Anti-Reflective Coating Reactive Ion Etching 60
3.3.2 Chromium Hard-Mask Wet Etch 61
3.3.3 Tungsten Reactive Ion Etching 63
3.4 Summary 67

4 Summary **69**
4.1 Summary of Accomplishments 69
4.2 Recommendations for Future Investigations 70

List of Figures

1.1 Diagram of a basic TPV system 12

1.2 Comparison of blackbody spectra for various temperatures, and the percentages of the 1500K black-body spectrum that fall within absorption spectra of various PV diodes 15

1.3 An improved TPV system including a spectral control component 15

1.4 Some avenues of TPV spectral control (the avenue pursued in this research is highlighted in black) 17

1.5 Room temperature emittance of tungsten based on reference refractive index values [17] 18

1.6 Examples of periodic variations of refractive indices in 1D, 2D and 3D . . . 19

1.7 Critical dimensions in a 2D round-hole PhC 20

2.1 Simulated room-temperature normal emittance from an array of cavities ($2r$ = 900nm, d = semi-infinite) in single-crystal tungsten based on reference optical properties of flat crystalline tungsten [12] 25

2.2 Scanning electron micrographs and critical dimensions of the selective emitter prototypes. Wall slant is defined as the ratio of the lateral and the vertical wall displacement. 26

2.3 Illustration of wall slant calculation 27

2.4 Comparison of atomic force micrographs of prototypes 1 and 3. Surface smoothness is visibly improved. 28

2.5 Experimental set-up for Cary 5E spectrophotometer near-normal reflectance measurement (not to scale) 30

2.6 Experimental set-up for Cary 5E spectrophotometer variable-angle reflectance measurements (not to scale) 30

2.7 Flat single-crystal tungsten emittance calculated from reference optical properties [12] and measured by the Cary spectrophotometer. 31

2.8 Flat single-crystal tungsten emittance calculated from reference optical properties [12] and flat poly-crystalline tungsten foil emittance measured by the Cary spectrophotometer. 31

2.9 Measured and simulated normal emittance for Prototype 1 33

2.10 Prototype 1 measured emittance for several angles 33

2.11 Measured and simulated normal emittance for Prototype 2 34

2.12 Prototype 2 measured emittance for several angles 34

2.13 Measured and simulated normal emittance for Prototype 3 35

2.14 Prototype 3 measured emittance for several angles 35

2.15 Prototype 1: Comparison of energy delivered by black-body and by the selective emitter 38

2.16 Prototype 1: Comparison of energy delivered by black-body and by a combination of black-body, selective emitter, and dielectric stack mirror 38

2.17 Prototype 2: Comparison of energy delivered by black-body and by the selective emitter 39

2.18 Prototype 2: Comparison of energy delivered by black-body and by a combination of black-body, selective emitter, and dielectric stack mirror 39

2.19 Prototype 3: Comparison of energy delivered by black-body and by the selective emitter 40

2.20 Prototype 3: Comparison of energy delivered by black-body and by a combination of black-body, selective emitter, and dielectric stack mirror 40

2.21 Basic assembly for FTIR high-temperature emission measurement (not to scale) 42

2.22 Ceramic heater mounted to a stand, as viewed from the vacuum chamber port. 44

2.23 Sample and sample holder as seen through the window of the vacuum chamber. 44

2.24 Full FTIR emissions assembly, with vacuum hose and gauge visible on the left, and the temperature control and electrical supply leads on the right. The chamber is mounted on a three-axis adjustable stand. 44

2.25 Flat tungsten high-temperature FTIR emission measurement for several temperatures 45

2.26 Tungsten selective emitter (Prototype 1) high-temperature FTIR emission measurement for several temperatures 45

2.27 Tungsten selective emitter (Prototype 1) FTIR emission measurement at 1100°C and prototype 1 room-temperature measurement coupled into black-body radiation at 1100°C 46

2.28 Flat tungsten emittance at room-temperature [12] and 1500K [44] 46

2.29 Prototype 1 ratios of selective emitter and flat tungsten measurements at 1100°C (measured by FTIR), room temperature (measured by Cary spectrophotometer), and room temperature simulations 48

2.30 Prototype 3 after oxidation damage at high-temperature 48

3.1 Fabrication process steps 50

3.2 Fabrication process flow 51

3.3 Schematic of the Lloyd's mirror laser interference lithography equipment set-up 52

3.4 Incident and reflected wave interference in a Lloyd's mirror system 53

3.5 Interference of two TE waves incident at angle θ forming a pattern on the $x-y$ plane 53

3.6 Decomposition of an incident sinusoidal wave into the horizontal (desired) and vertical (undesired) components 54

3.7 Exposure process: a) first lithography exposure; b) second lithography exposure at 90° from the first; c) resulting lithographic pattern. 54

3.8 Proximity effect is observable when the feature size approaches resolution limits. The shape of each feature is influenced by its distance from other features. 54

3.9 Relationship of the hole diameter, roundness, wall thickness, and exposure time, for a laser power of 170 μW. 55

3.10 Vertical interference resulting from reflective hard-mask surface 56

3.11 Scanning electron micrographs (SEMs) showing exposure results in photoresist (PR) with an ARC layer (left) and without an ARC layer (right) . . . 56

3.12 The PS4 photoresist layer thickness as a function of constant rpm for 60 seconds of spinning. 57

3.13 The BARLi ARC layer thickness as a function of constant rpm for 60 seconds of spinning. 57

3.14 Percent of reflected power for transverse electric (TE) and transverse magnetic (TM) waves as a function of the thickness of the anti-reflective coating (ARC) layer. Notice that minima exist for TE and TM reflection around 240 nm of ARC thickness. 58

3.15 SEM images of top (left) and edge (right) views of the developed sample pattern after a double (2D) 80-second exposure at 0.25 μW and a one-minute PR development in CD-26 developer 59

3.16 Triple exposure: a) with exact offset angle control - notice uniformity of intersections throughout the whole exposure area; b) with slightly different offset angles between exposures - notice that the three exposures do not intersect uniformly. 59

3.17 Triple exposure laser interference lithography SEM: a hexagonal pattern of round holes is formed in photoresist wherever the three exposure directions intersect properly. 60

3.18 ARC RIE calibration experiments at 140-145 W RF power and 240-245 V DC bias 62

3.19 SEM images of top (left) and edge (right) views of ARC on top of chromium hard mask, after the ARC etch in He/O_2 for 3 minutes and 30 seconds . . . 63

3.20 SEM images of etched chromium hard-mask on top of tungsten substrate (prototype 1): top (left) and edge (right). Chromium hard-mask was removed during a one-minute etch in Cyantek CR-7. The ARC layer was removed using He/O_2 RIE. 63

3.21 Diluted CR-7 etch with experimental points and trendline. Chromium thickness was held constant at 50nm. 64

3.22 Comparison of CR-7 wet etch results for chromium layers deposited in uncleaned, high-pressure deposition chamber conditions (left) and cleaned, low-pressure deposition chamber conditions (right) 64

3.23 Initial tests of tungsten RIE with varying durations 65

3.24 Depth etched into single-crystal tungsten for various tungsten RIE power and pressure 66

3.25 Remaining chromium mask thickness in single-crystal tungsten RIE experiments with varying power and pressure 66

3.26 SEM images of prototype 1 tungsten RIE progress over time (edge views at 60°) 68

3.27 SEM images of prototype 3 tungsten RIE progress over time (edge views at 75°) 68

List of Tables

1.1 Summary of previous TPV selective emitter work 21

2.1 Simulation parameters and peak wavelength values for Prototypes 1-3 . . . 32

2.2 Additional loss mechanisms, not included in current simulations 36

2.3 Combined spectral efficiencies of the dielectric stack mirror and selective emitter prototypes based on room-temperature measurements and extrapolated to 1500 K black-body radiation 41

2.4 Spectral efficiencies of the selective emitter prototypes based on room-temperature measurements and extrapolated to 1500 K black-body radiation (without the dielectric stack mirror) 42

3.1 Parameters for the reflectance simulation 58

3.2 Parameters for ARC and photoresist spinning and baking 58

3.3 Tungsten RIE test results for various power and pressure combinations . . . 67

Chapter 1

Introduction

This research investigates the fabrication, modeling, characterization, and application of two-dimensional (2D) photonic crystals (PhCs) as selective emitters and means of achieving higher efficiencies in combustion-driven thermophotovoltaic (TPV) systems. The main goal of this thesis is to evaluate the impact of 2D PhC-based selective emitters on TPV efficiency.

This chapter will introduce thermophotovoltaic systems, and present motivation for this research. The basics of TPV systems and avenues for improvement will be explored. We focus on tungsten selective emitters based on 2D PhCs as efficiency-driving components in TPV systems. The last section will summarize thesis contributions and outline chapter structure.

1.1 Thermophotovoltaic Systems

A basic TPV system (Fig. 1.1) consists of two parts: a thermal emitter and a photovoltaic (PV) diode. Thermal energy is provided to an emitting surface — the thermal emitter — which in turn radiates a spectrum of photons. The radiated photons are converted into free charge carriers when absorbed by the PV diode. This two-step process is the core of the TPV power conversion principle. The concept is similar to solar energy conversion, the main differences being a lower temperature source instead of the sun, and a very short distance between the source and the PV diodes.

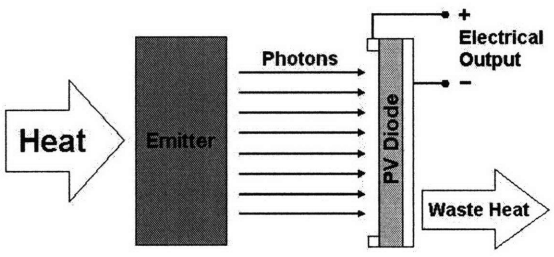

Figure 1.1: Diagram of a basic TPV system

The inception of the TPV technology is somewhat obscured by the shroud of time. Until recently, it was widely believed that it was Dr. Pierre Aigrain who first proposed this technology while a visiting professor at MIT in the fall of 1960 [1]. Some further investigations showed that Aigrain may have suggested this idea as early as 1956 [2]. According to the most recent findings Aigrain may have gotten the idea from Dr. Henry H. Kolm, of MIT Lincoln Laboratory [3]. The undocumented chain of human interactions makes it difficult to claim with absolute certainty who is the parent of this technology. However, a recently found 1956 report written by Kolm is thus far the oldest document mentioning this technology [4].

Although TPV systems have been investigated for over 50 years, they have yet to see widespread commercialization. The main obstacles to commercialization of TPV systems are their low efficiency and high cost. In the early stages of TPV development in the 1960's, the simple coupling of a thermal emitter and a germanium PV cell yielded 1% as its highest fuel-to-electricity efficiency [5, 6]. Although the emitter radiates a powerful spectrum, that spectrum is very broad and its intensity is largely mismatched with the sensitivity spectrum of the PV diode. In order to achieve higher TPV efficiencies it is necessary to better match the emitted spectrum to the sensitivity spectrum of the diode. Spectral control and development of low-bandgap PV diodes, therefore, became the objectives of much research in this area. However, the efforts yielded little results as both the diode and spectral control technologies were severely limited at the time.

It was the development of material and fabrication technologies during 1980's and 1990's that enabled further advances in PV diode and spectral control designs for TPV systems. While many significant improvements have been made in the PV diode designs, we will focus on spectral control issues for the remainder of this document. Let us now consider the relevant details of the emitter and the diode operation.

1.1.1 Emitter

Most naturally-occurring emitters can be modeled as partially efficient black-bodies, for which the photon distribution across the frequency spectrum is dictated by Planck's Law:

$$E(T,\lambda) = \frac{2\pi h c_o^2}{n^2 \lambda^5 (e^{\frac{hc_o}{\lambda kT}} - 1)} \tag{1.1}$$

Planck's black-body radiation law states that the amount of radiated energy (E) for a given temperature (T) and wavelength (λ) is dependent on the wavelength, the material properties of the partially-efficient black-body (through n, the real part of the refractive index), and the temperature of the black-body, and scaled by the Planck's constant (h), π, and speed of light in vacuum (c_o).

As the black-body temperature increases, the radiated spectrum increases in intensity and shifts towards shorter wavelengths. This dependence of the radiated spectrum on temperature permits us to use temperature to manipulate the position of the spectrum's peak. The extent to which the operating temperature can be used to manipulate the radiated spectrum is limited by practical considerations, such as emitter packaging and thermal management.

1.1.2 PV Diode

PV diodes are semiconductor devices that interact with incident photons of certain energies. The semiconductor material of which the diode is made, for example silicon (Si), exhibits a natural energy band-gap determined by the material's atomic structure. An electron or hole may traverse the energy band-gap if provided with energy at least equal to the band-gap energy (E_g). This energy can, for example, be provided by a sufficiently energetic incident photon.

A silicon PV diode has E_g of 1.1eV, corresponding to a wavelength λ_g of 1.1 μm. From Fig. 1.2 it is evident that for T < 1500K only a small percentage of the radiated photons are emitted at wavelengths shorter than 1.1 μm. The pairing of a silicon diode and the shown emittance spectra would lead to a very inefficient TPV system because the silicon diode would make use of only a very small portion of the radiated spectrum. An increase in the emitter temperature would shift the emitter spectrum towards shorter wavelengths, thereby increasing the system's efficiency. However, an increase in temperature would make thermal management of the system even more difficult. An alternative is to use a PV diode with a lower energy band-gap, that is, longer wavelength λ_g.

PV diodes can be fabricated from a variety of materials. Some PV diodes have very small band-gap energies (such as quaternary materials as InGaAsSb) and are sensitive to a greater portion of the blackbody spectrum, leading to a higher TPV system efficiency. However, such diodes' cost is high and prohibitive to low-cost system implementation, despite the increase in system efficiency due to the increased sensitivity of the diode.

Gallium antimonide (GaSb, E_g = 0.72 eV, λ_g = 1.77 μm) has prevailed as the material of choice for PV diodes in TPV systems [8]. The material has a low-energy direct band-gap that makes use of a larger number of incident photons. Additionally, the material lends itself to relatively easy PV diode fabrication using commercial fabrication processes [9].

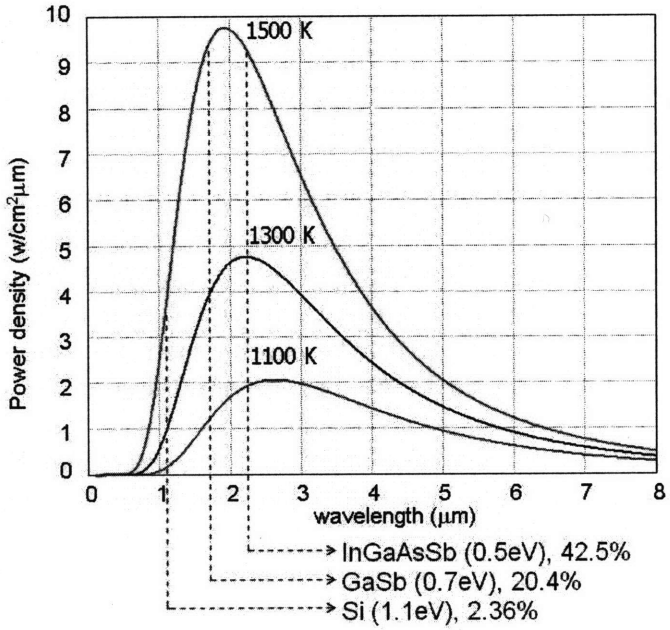

Figure 1.2: Comparison of blackbody spectra for various temperatures, and the percentages of the 1500K black-body spectrum that fall within absorption spectra of various PV diodes

1.1.3 System Efficiency

Even with its small energy band-gap, GaSb PV diodes can make use of only a small portion of a black-body spectrum, as shown in Fig. 1.2. This spectral mismatch calls for better matching between the emitted spectrum and the spectral sensitivity of the diode. Spectral control serves to prevent insufficiently energetic photons from reaching the diode, thereby keeping the PV diode cool and functioning at peak efficiency. An improved TPV system with a spectral control component is shown in Fig. 1.3.

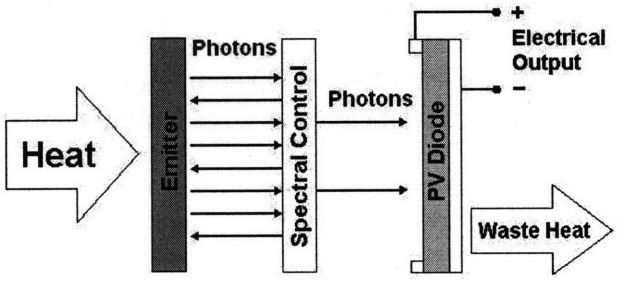

Figure 1.3: An improved TPV system including a spectral control component

To achieve high system efficiency, high spectral control efficiency is required. There are two quantities that speak to the quality of a spectral control component: 1) the amount of

energy below the band-gap wavelength with respect to the total energy radiated by the emitter across the entire wavelength spectrum (spectral efficiency), and 2) power radiated below band-gap wavelength with respect to black-body power below band-gap wavelength at the same temperature (in-band power density). High in-band power density means that the selective emitter is radiating close to the power radiated by the black-body at the same temperature. For high overall spectral efficiency only the photons with energies equal to or greater than the band-gap energy should be allowed to reach the PV diode, and their total energy should be as close to the maximum theoretical black-body energy for that particular operating temperature. In the wavelength domain, this means that only the photons with wavelengths equal to or shorter than the band-gap wavelength of the semiconductor will form the convertible portion of the spectrum.

With the introduction of a spectral control component, the overall TPV system efficiency can be approximated by the product of the emitter efficiency (η_E), the spectral control component efficiency (η_{SC}), and the PV diode efficiency (η_{PV}):

$$\eta_{TPV} = \eta_E \cdot \eta_{SC} \cdot \eta_{PV} \tag{1.2}$$

The efficiency of the emitter is defined as the ratio of the radiated energy to the chemical energy used to heat the emitter. The PV diode efficiency is defined as the ratio of the electrical energy output to the photon energy incident upon the diode.

Previous research has investigated various spectral control methods, of which an extensive review is given in [1]. Common spectral control methods are shown in Fig. 1.4. Spectral control components are often classified as cold-side or hot-side. The cold-side components are installed near or on the PV diode. Such spectral control components operate near room temperature, and are usually filters (selective mirrors) or anti-reflective coatings on the PV diode. Previous work by our research group has produced simple, yet highly-efficient 1D PhC filter tailored for use with GaSb PV diodes [10].

The hot-side spectral control components are installed upon or integrated into the emitter. These components operate at elevated temperatures (at or close to the temperature of the emitter), and are often termed *selective emitters*. The main topic of this research is the development and fabrication of highly efficient selective emitters based on 2D PhCs, a route which is highlighted in Fig. 1.4.

1.2 Spectral Control Via Selective Emitters

Selective emission is defined as strong emission at some frequencies and weak emission at others. Particularly, selective emitters are thought of as a "class of materials whose

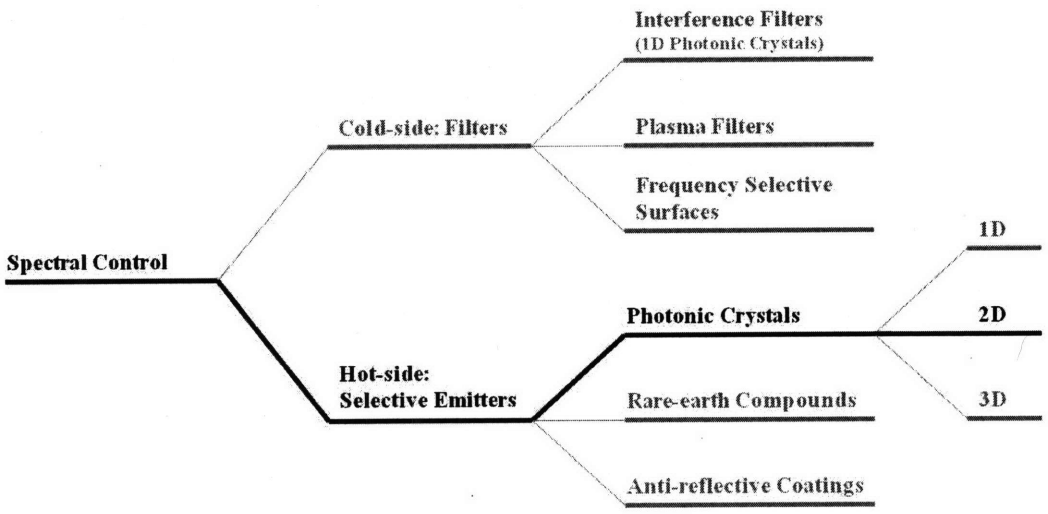

Figure 1.4: Some avenues of TPV spectral control (the avenue pursued in this research is highlighted in black)

thermal-radiation emission at equilibrium (or in a steady state not far from equilibrium) occurs in a much narrower spectral region compared to a black-body at the same temperature" [11]. In nature, we find two sources of selective emission: intrinsic material properties and physical structuring.

1.2.1 Selectivity Due to Material Properties

Theory and experiments have shown that the refractive index of a material changes sharply at frequencies that resonate with the natural frequency of the material's chemical bonds [12]. The variations in the refractive index are observable for virtually all known materials when a wide wavelength range is considered. Wavelength-dependent refractive indices lead to wavelength-dependent optical properties, including emission. Some examples of materials with sharply varying refractive indices that result in selective emission suitable for TPV applications are rare-earth oxides, such as holmium (Ho) or erbium (Er) oxide, and transition metals, such as hafnium (Hf) or tungsten (W).

The spectra of rare-earth ions have shown narrow bands of radiation, much narrower than most other solid materials [13]. Of the rare-earth elements, the emittance spectra of erbium and ytterbium were found particularly useful as their peaks occur at energies above the band-gap energies of most PV diode materials [14]. Research efforts still attempt to develop highly efficient selective emitters for TPV applications [15, 16]. These efforts have mainly focused on using arrays of micrometer-length filaments. Such selective emitters are structurally stable at elevated temperatures, but provide very low power densities and their manufacturing processes prove complicated [16].

The refractive index variations of certain transition metals have properties particularly suitable for TPV applications using GaSb PV diodes. In particular, the refractive index of tungsten provides for increased emittance at wavelengths shorter than 2μm, and suppressed emittance at longer wavelengths [12]. Figure 1.5 shows normal emittance from flat-surface tungsten at room temperature.

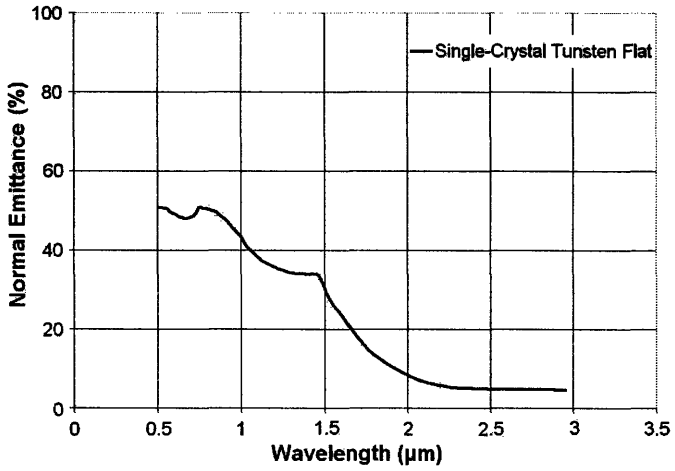

Figure 1.5: Room temperature emittance of tungsten based on reference refractive index values [17]

Although planar single-crystal tungsten exhibits only mild selective emittance properties, it makes a highly suitable substrate for selective emitters with more pronounced selective emission properties. Because of its refractive index, and excellent thermo-mechanical properties (melting temperature of 3422°C), tungsten is the choice of substrate material for the 2D PhC-based selective emitters studied in this research. As will be shown subsequently, the emissivity of tungsten can be modified significantly by the introduction of a periodic pattern to its surface. This modification is beneficial because it increases short-wavelength emissions, while preserving low emissions at longer wavelengths. Besides the physical structuring that will be explained shortly, two important properties of tungsten should be noted at this time.

Firstly, tungsten comes in two distinct forms from an optical standpoint: crystalline and amorphous. The emission spectrum presented in Fig. 1.5 is based on the properties of single crystal tungsten. Amorphous tungsten does not exhibit the selective emission properties of its single-crystal counterpart. Moreover, in the course of our investigation, poly-crystalline tungsten foil was found to have much of the optical properties of single crystal tungsten. Results of poly-crystalline foil characterization are included in Chapter 2.

Secondly, at elevated temperatures the refractive index of single crystal tungsten increases at longer wavelengths [18]. This refractive index increase leads to more intense emission at longer wavelengths and decreases the appeal of single crystal tungsten as a selective emitter substrate. However, our simulations estimate that the increase in emission at longer

wavelengths is much weaker than the emission at shorter wavelengths, that is, tungsten preserves most of its selective emission properties; this estimate is indeed confirmed by our experimental results, discussed in Sec. 2.5.

1.2.2 Selectivity Due to Physical Structuring

Besides intrinsic material properties, another path towards selective emission uses physical structuring of the material to induce selective spectral behavior. Such structures often consist of periodic layers of alternating materials, posts or holes (cavities) etched into the surface of the substrate materials, or three-dimensional volumes with crystalline structure. All of these structures are collectively referred to as photonic crystals (PhCs). A PhC is a structure with spatially-periodic variations of the refractive index, where the variation period is on the order of the wavelength of interest [19]. The variation of the refractive index can occur in one, two or three dimensions, resulting in one- (1D), two- (2D), or three-dimensional (3D) PhCs, respectively. Some of the possibilities for refractive index variations are illustrated in Fig. 1.6, where light and dark areas represent blocks of materials of low and high refractive indices. The contrast between the refractive indices and the material volume proportions are the two variables that define the spectral properties of a PhC. All three kinds of PhCs occur in nature, but it was not until recently that developments in fabrication techniques have enabled production of artificial PhCs on the same scales as those occurring naturally.

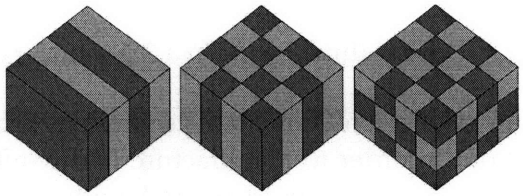

Figure 1.6: Examples of periodic variations of refractive indices in 1D, 2D and 3D

The earliest observation of a PhC was reported by Lord Rayleigh in 1917 [20]. The focus of his investigation was the reflection of light from skeletal coatings of certain insects. These skeletal coatings are laminar in structure, consisting of a few layers of materials with sharply varying refractive indices. The reflection from such coatings resulted in the refraction of light depending on the incident angle. This publication provided a first insight into the performance of dielectric stack mirrors or 1D PhCs. The findings were not given much attention at that time partly because there were no techniques by which such a structure could be artificially reproduced and further analyzed. The development of planar material evaporation and deposition techniques during the late 20^{th} century that rekindled the interest in such dielectric structures.

Theoretically speaking, 3D PhCs offer the most efficient selective emission performance [21, 22]. However, the techniques for their fabrication are significantly more complicated, time-consuming and expensive [23]-[25]. These complexities of 3D PhC fabrication offset the attractiveness of their optical performance. Hence, let us focus on the 2D family of PhCs.

1.2.3 Synergy of Material Properties and Physical Structuring

In nature, 2D PhCs have mainly developed for two purposes: iridescence and anti-reflection coatings. In Aphrodita sp. or Sea mouse a 2D hexagonal PhC of its hairs gives the creature a slight reddish iridescence [26]. Moth eyes are another example of a 2D PhC in nature, in which case the hexagonal 2D PhC acts as an anti-reflection coating for the moth's large eyes and aids the insect in camouflage [27].

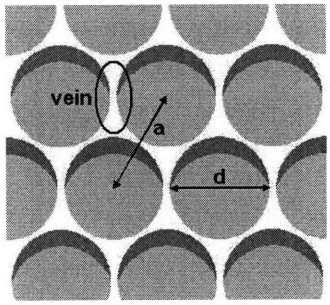

Figure 1.7: Critical dimensions in a 2D round-hole PhC

Since the rapid development of microfabrication technology during the 1980's, copious research has been carried out in order to manufacture highly-efficient selective emitters. Table 1.1 contains some of the most-referenced research with details as to types of emitters, filters, and diodes. Comparison of research efforts is difficult as efficiency measurements for TPV systems have not been standardized as of the time of this thesis. However, spectral efficiencies of 85-90% (at room-temperature) are the maximum achieved efficiencies reported in literature at this time [8, 37].

As with any selective radiation source, the main challenge lies in achieving near-unity and near-zero emittance in desired wavelength ranges, as well as a steep transition between those ranges. In reality, a selective emitter is limited by the material from which it is made. Single-crystal tungsten is highly-suitable for this application, and our selective emitter design makes the most of tungsten's natural optical properties.

The features used for our selective emitter are round low-permittivity columns (holes or cavities) of diameter d inside a high-permittivity medium. The period of the structure is defined as the distance between the centers of the low-permittivity columns, and is marked a in Fig. 1.7. Structure period, the ratio of the column dimensions to the column spacing

Table 1.1: Summary of previous TPV selective emitter work

Emitter	Temperature	Fabrication	Filter	Diode	Efficiency	Reference
Silicon carbide	1500K	*Simulation*	*NR**	GaSb/GaAs	26% [1]	[8]
Rare-earth oxides	1500-2000K	*Simulation*	*NR*	*NR*	75% [2]	[28]
Radio-isotope	1300-1500K	*NR*	*Mesh Filter*	GaSb	10-16% [3]	[29]
Tungsten, with ARC[5]	1150K	*Simulation*	*1D PhC*	GaSb	10.8% [3]	[30]
Silicon, inverse pyramids	*NR*	*E-beam*[6]	*Platinum*	*Varies*	*NR*	[31]
Silicon, square holes	738-769K	*E-beam*[6]	*None*	*NR*	*NR*	[32]
Tungsten, square holes	1180-1700K	*E-beam*[6], *FAB*[7]	*None*	GaSb	*NR*	[33]
Tungsten, round holes	1500K	*LIL*[8], *RIE*[9]	*Haffnia ARC*[5]	GaSb	*NR*	[34]
Silicon, round holes	600K	*Deep RIE*[9]	*Metal ARC*[5]	*NR*	*NR*	[35]
Silicon carbide	1300K	*NR*	*1D PhC*	InGaAs	23.6% [4]	[36]
NR	1230K	*NR*	*Tandem*[10]	InGaAsSb	83%[11]	[37]

(*) *Not reported (NR)*

(1) *Simulated fuel to electricity efficiency*

(2) *Simulated spectral efficiency*

(3) *Measured fuel to electricity efficiency*

(4) *Measured radiation to electricity efficiency*

(5) *Anti-reflective coating (ARC)*

(6) *E-beam lithography is orders of magnitude slower than LIL*[8]

(7) *Fast-atom beam etching (FAB)*

(8) *Laser interference lithography (LIL)*

(9) *Reactive ion etching (RIE)*

(10) *Dielectric mirror and plasma interference filter*

(11) *Measured spectral efficiency*

(d/a), and the choice of substrate material determine the structure's radiative behavior. Detailed presentation of selective emitter theory and simulation is given in [38]. Simulations and results specific to the cavity-based prototypes fabricated for this research are given in Chapter 2.

Although there is some selectivity in emittance of planar single crystal tungsten, it is not a true selective emitter due to weak overall emittance. However, combined with a pattern of microfabricated cavities, a block of single crystal tungsten can become a powerful selective emitter amenable to a variety of applications.

1.3 Contributions and Structure

The contributions of this thesis can be classified into two categories: microfabrication of selective emitters and TPV system improvements. These contributions provide a leap towards higher TPV system efficiency:

(1) characterization of the tungsten reactive ion etching process,

(2) design of simplified and faster processing of tungsten PhCs compared to previous work,

(3) development of a complete process recipe for fabrication of 2D PhC tungsten selective emitters,

(4) fabrication of several selective emitter prototypes to design specification,

(5) measurement of room-temperature spectral efficiency in excess of 90%, and

(6) experimental evaluation of selective emitters at temperatures over 1000°C.

In the remainder of this work, the reader will find a comprehensive evaluation of tungsten-based 2D PhC selective emitters for TPV, starting with the evaluation methods, experimental results, and simulation agreement (Chapter 2). Chapter 3 will detail the fabrication investigations, methods, and final recipes used in the production of the selective emitter prototypes. The thesis will conclude in Chapter 4 with a summary of accomplishments and recommendations for future investigations.

Chapter 2

Results

This chapter presents the theory, simulations, and measurement results of 2D PhC-based tungsten selective emitter prototypes. First, the basic mechanisms behind selective emission are introduced, and the essential design questions are answered. A brief presentation on simulation methods is included. The remainder of the chapter details physical and optical measurements, and their agreement with analytical results. Various characterization methods that are used for optical evaluation are presented. In addition, dimensional measurements of the fabricated prototypes are discussed with respect to design specifications. Room-temperature spectral measurement results follow, accompanied by a discussion of agreement between measured and simulated values. Finally, high-temperature prototype behavior and spectral measurements are analyzed. The chapter ends with a summary of accomplishments.

2.1 Theory

The theory behind cavity-based thermal emitters brings together a number of scientific disciplines. An exhaustive presentation of thermal emitter theory is given in [38]. There are three main mechanisms that influence the radiative behavior of a selective thermal emitter based on an array of cavities: surface plasmon, diffraction, and resonant cavity effects.

The surface plasmon mechanism exhibits narrow, angle-dependent peaks [32] and is only relevant in very shallow structures (where the depth of the structure is much smaller than its period). Diffraction phenomena can be observed in all periodic structures, where the period of the structure is comparable to the wavelength of incident light. Rainbows are a familiar natural example of diffraction. Cavity resonances are similar to waveguides, in that they have cut-off wavelengths below which no propagation of electromagnetic field is permitted.

Two of the mechanisms – diffraction and surface plasmon – are not dominant in our particular structures [39]. Therefore, the cumulative behavior of electromagnetic cavities dominates the overall behavior of our selective emitter design. Electromagnetic radiation from a finite-depth cavity is given by the following formula for resonant frequency ω_n [38]:

$$\omega_n = \sqrt{\left(\frac{lr}{4d}\right)^2 + \left(\frac{\xi_{mn}}{2\pi}\right)^2} \tag{2.1}$$

where d is the cavity depth, r is the cavity radius, l is an integer number, and ξ_{mn} is the n^{th} root of the m^{th} order Bessel function [38]. Based on the knowledge of cavity behavior, the parameters of 1000 nm for the period and 900 nm for the cavity, or hole, diameter were selected based on simulation results. However, a 900 nm diameter would leave only 100 nm for the walls between the cavities, which would be too thin for the available microfabrication techniques. In order to avoid wall puncturing in the fabrication process, we modified our design to aim for 800 nm cavity diameters and 200 nm walls between them.

While the intense selective emission behavior at short wavelengths is governed by the resonant cavities, the planar surface area between cavities determines the behavior at longer wavelengths. Independence of ω_n on the period of the structure might influence one to conclude that the pattern period is of no consequence. While the pattern of holes has no effect on the cavity behavior, it can deeply affect the structure's emittance at longer wavelengths. Extensive investigations [32, 33] have shown the effects of varying period and cavity dimensions on the overall behavior of the structure. While a pattern of closely-spaced (dense) cavities enhances short-wavelength radiation, it also increases radiation at longer wavelengths. Widely spaced cavities would result in less radiation at longer wavelengths, which may be desirable. However, a widely-spaced pattern of cavities also results in less radiation at shorter wavelengths, which is decidedly undesirable for this selective emitter design.

For a square pattern of holes approximately half of the selective emitter surface is composed of planar tungsten. While this is of insignificant influence for short wavelengths, above resonant cavity cut-off mode the density of cavities provides the upper performance limit for wavelengths much larger than the radius of the cavities [38]. The proportion of tungsten and cavities in the emitter surface gives us the upper limit on the effective dielectric constant of the structure, using effective medium theory [40]:

$$\epsilon_{eff} \leq p * \epsilon_W \tag{2.2}$$

where p is the proportion of the emitter's surface consisting of flat tungsten, and ϵ_{eff} and ϵ_W are the dielectric constants of the effective medium and of tungsten, respectively. For example, a square lattice structure with 1000 nm periodicity and 800 nm hole radii, has p of 0.51. Therefore, with a simple reflectance calculation modifying the flat tungsten refractive index by a factor of 0.51, we see that the emittance increases by a factor of 1.9 for the 2.2-5 μm wavelength range. In other words, while a flat tungsten surface has emittance in the range of 4-5% for wavelengths 2.2-3.3 μm, a tungsten surface with holes comprising 0.49 of the area will have emittance in the range of 7-10%.

2.2 Simulations

Initial simulations were crucial in determining the potential of 2D PhC-based tungsten structures as selective emitters. The simulations were conducted using the finite element method (FEM) electromagnetic software package HFSS [41]. This powerful software tool enabled the investigation of the selective emission possibilities of for the 2D PhC-based structure.

The initial simulation was conducted for a 1 μm-period square-pattern 2D PhC in tungsten. The hole diameter was 900 nm, and the depth was semi-infinite. The tungsten refractive index values were taken from [12]. The normal emittance characteristic for this structure is shown in Fig. 2.1.

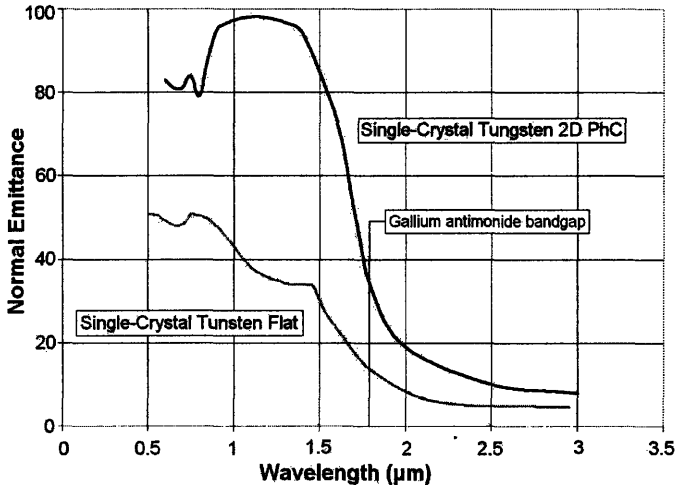

Figure 2.1: Simulated room-temperature normal emittance from an array of cavities ($2r$ = 900nm, d = semi-infinite) in single-crystal tungsten based on reference optical properties of flat crystalline tungsten [12]

The selective emitter behavior shown in Fig. 2.1 is particularly suited for TPV systems with GaSb PV diodes. Firstly, the peak emittance for shorter wavelengths exceeds 90%. Secondly, the emittance dips below 10% for wavelengths longer than 2.5 μm. Thirdly, the transition from 80% to 20% emittance occurs over less than 0.4 μm of wavelength and crosses 50% at 1.7 μm, which is the cut-off wavelength for GaSb PV diodes. For longer wavelengths, it is also important to note the simulation's agreement with the prediction of increased emittance (about a factor of 2) due to decreased tungsten surface area (2.2).

The three characteristics listed above are in line with the expectations of a selective emitter tailored for a particular application, as discussed in Sec. 1.2.3. With the simulated confirmation of our theoretical expectations, we have set out to produce prototypes and examine their real behavior. The next sections present the range of prototypes produced, their

room- and high-temperature performance, and discusses the agreement between theory and simulations.

2.3 Dimensional Characterization

During the course of this research three prototypes were fabricated. A summary of prototype dimensions and their corresponding scanning electron micrographs (SEMs) are shown in Fig. 2.2. The scanning electron microscope was Zeiss model 982, located in the MIT NanoStructures Laboratory (NSL). Hole diameter was measured at hole opening, and wall slant was calculated as the ratio of the lateral offset at the wall's base and the wall's height (see Fig. 2.3).

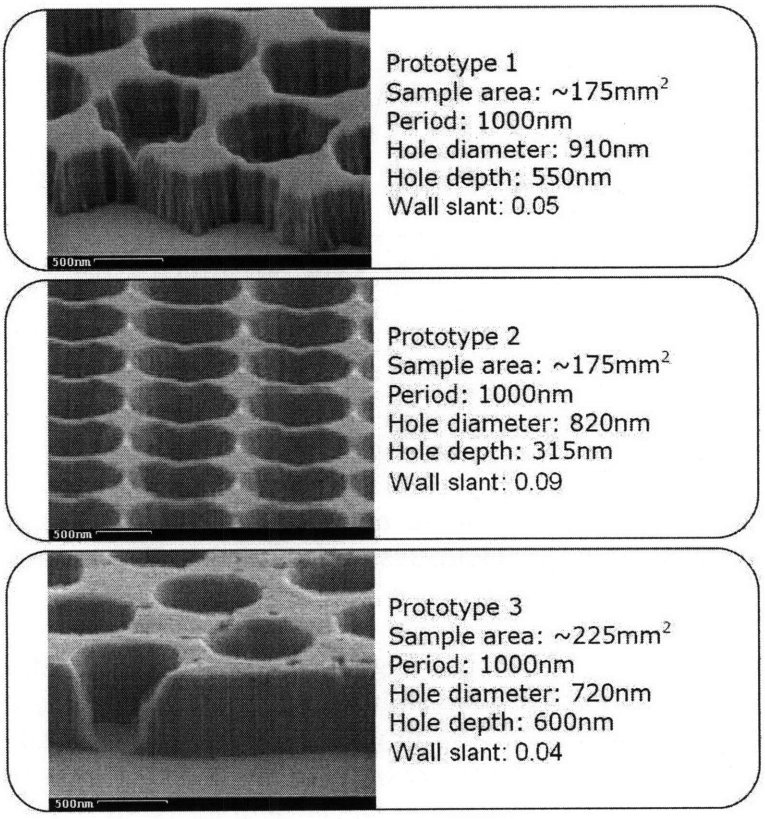

Figure 2.2: Scanning electron micrographs and critical dimensions of the selective emitter prototypes. Wall slant is defined as the ratio of the lateral and the vertical wall displacement.

Prototype 1 shows excellent agreement with dimensional specifications. However, the shape of the hole sidewalls is quite rough. The prototypes 2 and 3 improved upon pattern precision and smoothness. The most striking improvement between the first and third

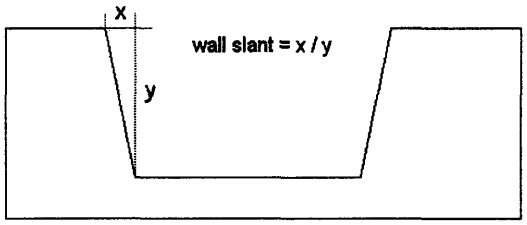

Figure 2.3: Illustration of wall slant calculation

prototype is the reduction of the rough sidewall features in the cavities. The improvement is mainly due to a better understanding of the materials and the fabrication processes used, a discussion of which is available in Sec. 3.3.2.

Although SEMs provide insight into the dimensions of the structure, a more accurate method was used to precisely measure the structures' features. Atomic force microscopy (AFM) tapping mode images of prototype 1 and 3 are shown in Fig. 2.4. Using the AFM cross-sectional and three-dimensional analysis tools, we were able to obtain the values given in Fig. 2.2. The simulations were then repeated using the newly obtained dimensions. The results of the iterated simulations for each prototype are presented in the next section.

2.4 Room-Temperature Spectral Characterization

The prototypes' room-temperature optical properties were analyzed using a Cary 5E near-infrared dual-beam spectrophotometer. The Cary spectrophotometer was used to determine the reflectance of the samples. The principle behind this spectrophotometer is that of comparison of a beam traveling through free space with the beam traveling through, or being reflected from, a sample. Hence, the *dual-beam* in the spectrophotometer's name.

Via the conservation of energy law, the reflectance measurement provided us information about the samples' emittances. According to the law, a sample's reflectance (R), transmittance (Tr), and absorbance (A) must collectively account for all energy impinged upon the sample:

$$1 = R + Tr + A \tag{2.3}$$

In addition, Kirchoff's Law [31] states that the emittance (ϵ) is equal to the absorbance for a given temperature (T) and wavelength (λ) (2.4). An extension of the Kitchoff's Law relates very simply the absorbance, reflectance and transmittance of the body (2.3). With

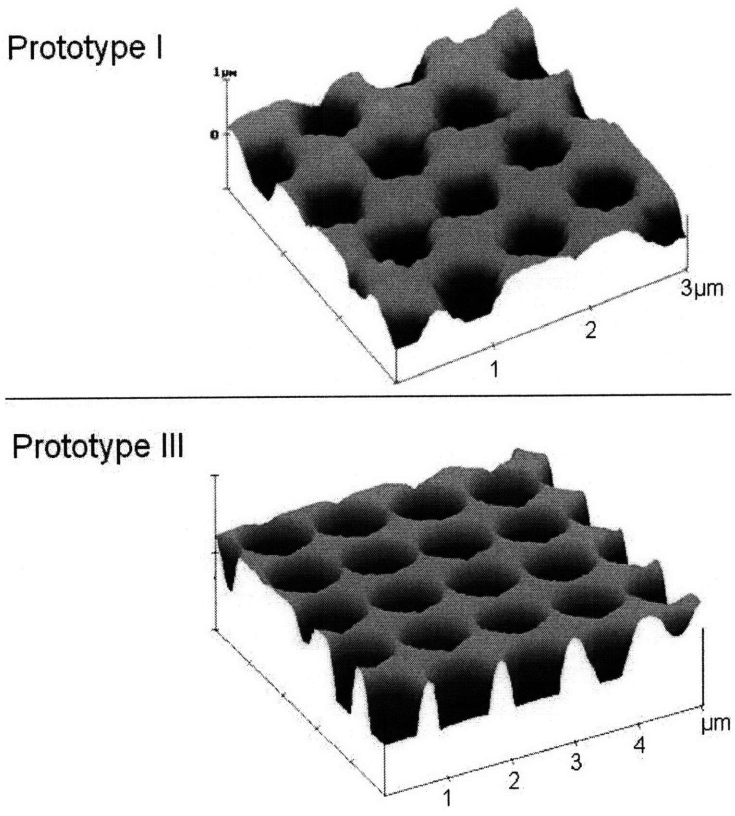

Figure 2.4: Comparison of atomic force micrographs of prototypes 1 and 3. Surface smoothness is visibly improved.

Kirchoff's law we can easily relate the reflectance/transmittance measurement to the emittance.

$$\epsilon(\lambda, T) = A(\lambda, T) = 1 - R - Tr \tag{2.4}$$

It is also known that the sample transmittance is zero in the wavelength range of interest (Tr = 0), leaving us with a very simple expression for emittance:

$$\epsilon(\lambda, T) = A(\lambda, T) = 1 - R \tag{2.5}$$

The Cary 5E specular reflectance accessory (SRA) was used to measure the near-normal reflectance properties of the samples. The experimental set-up is shown in Fig. 2.5. Due to the construction of the SRA, the minimum possible measurement angle is 7^o.

Another accessory – the variable angle specular reflectance accessory (VASRA) – was used to carry out the angled reflectance measurements. The VASRA has some similarities to the SRA, as can be observed by comparing Figs. 2.5 and 2.6. One important difference should be noted: the beam-paths in SRA are of comparable length (sample:reference=1.2:1), while in VASRA the sample beam-path is significantly longer than the reference beam-path (sample:reference=4.4:1). The difference in beam-paths is important to note because the Cary measurements are calculated based on the difference between the two paths. The VASRA beam-path difference manifests itself in measurements with pronounced atmospheric absorption peaks since the sample beam has to travel through atmosphere significantly longer than the reference beam. Even the slightest changes in atmosphere affect the measurement (when the sample compartment is opened to exchange samples, for instance). These absorption peaks are in the 2.56-2.94 μm wavelength range and are due to water vapor.

2.4.1 Flat Tungsten

Room-temperature optical properties of flat tungsten wafers were measured to examine agreement between our actual samples of tungsten and the reference [12] refractive index values that were used for our simulations. Cary SRA measurement shows overall agreement with reference values (Fig. 2.7).

Although there is overall agreement between measurement and reference, there are two wavelength ranges where the agreement is not exact. Firstly, in the 1.25-1.5 μm range, the reference values exceed the measurement. Secondly, in the 1.7-2.8 μm range, the reference values are much lower than the measurement. Inquiring into the possible causes of the disagreements, the purity of the material emerges as the main cause.

In addition to single crystal tungsten wafers, poly-crystalline tungsten foil was investigated as a low cost substrate option for selective emitters. Poly-crystalline tungsten foil is manufactured by alternating hot-cold rolls of bulk tungsten powder. Tungsten powder comes in a variety of grain sizes, up to 25 μm [42]. Cary SRA measurements of polished tungsten foil are shown in Fig. 2.8.

Overall, poly-crystalline tungsten foil has optical properties similar to single crystal tungsten. Slightly higher emittance, calculated based on reflectance measurements, can be attributed to scattering from the foil surface. Even though the foil is polished, it is not as finely polished as the single crystal tungsten wafers. Surface roughness results in lower reflectance, and therefore higher emittance calculation. At the time of this thesis, the price ratio of tungsten wafers and tungsten foil is about 1000:1 per unit surface, leaving abundant room for further foil processing such as flattening and polishing. If the foil were sufficiently flat and polished (comparable to wafers for microfabrication), tungsten foil could easily replace single crystal tungsten wafers and result in significant reduction in the cost of selective emitters.

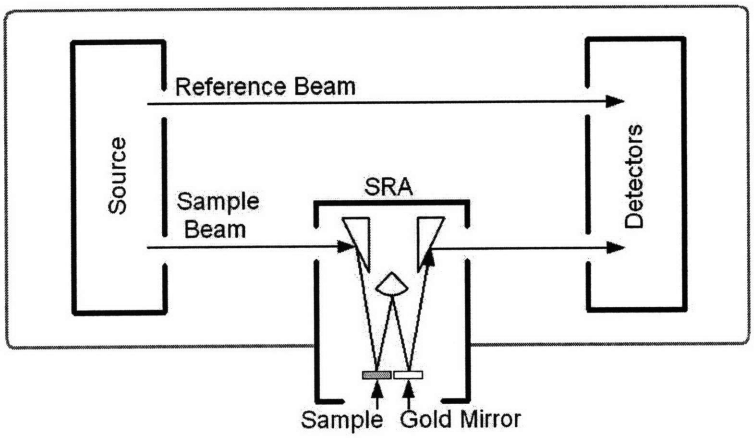

Figure 2.5: Experimental set-up for Cary 5E spectrophotometer near-normal reflectance measurement (not to scale)

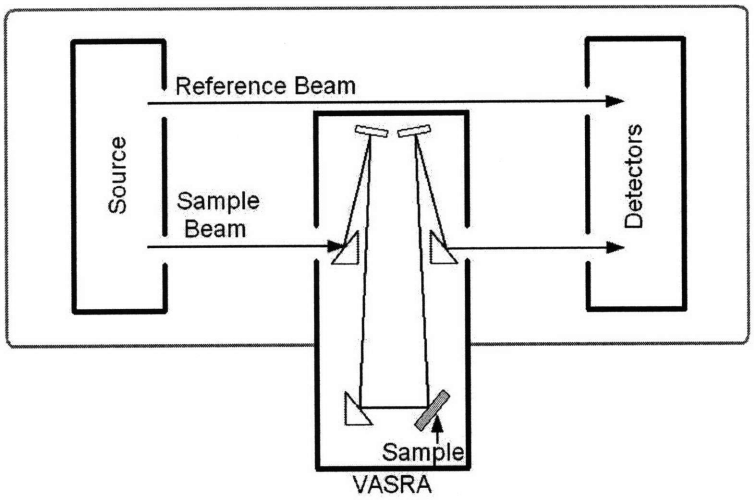

Figure 2.6: Experimental set-up for Cary 5E spectrophotometer variable-angle reflectance measurements (not to scale)

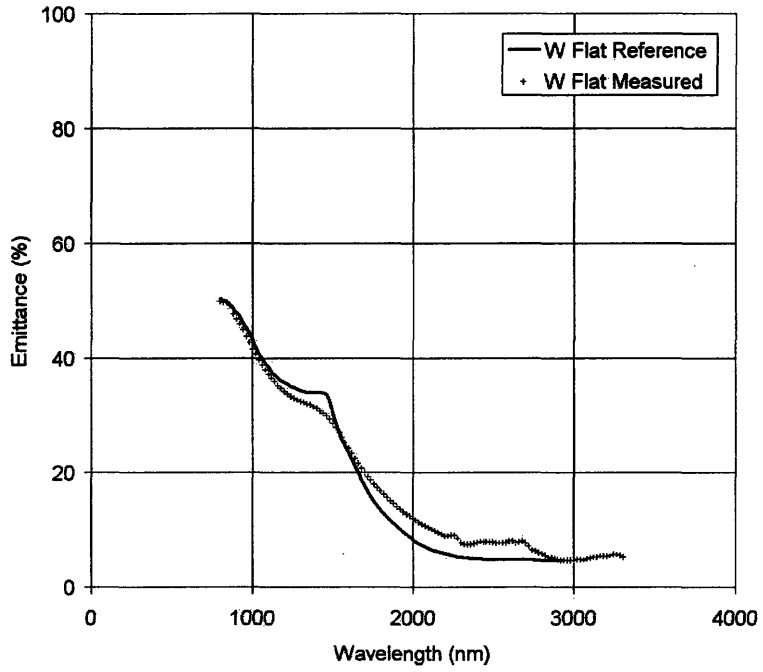

Figure 2.7: Flat single-crystal tungsten emittance calculated from reference optical properties [12] and measured by the Cary spectrophotometer.

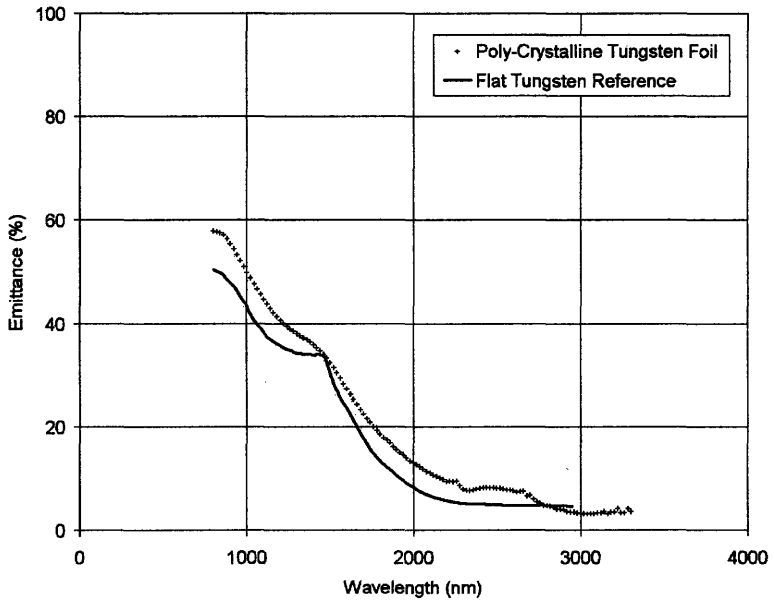

Figure 2.8: Flat single-crystal tungsten emittance calculated from reference optical properties [12] and flat poly-crystalline tungsten foil emittance measured by the Cary spectrophotometer.

2.4.2 Selective Emitter Prototypes

Cary SRA and VASRA room-temperature reflectance/emittance measurements were performed for each of the three prototypes. The comparisons of normal emittance simulations with measurements are shown in Figs. 2.9, 2.11, and 2.13. Angled emittance measurements are shown in Figs. 2.10, 2.12, and 2.14. Table 2.1 lists simulation parameters, and measured and simulated resonant frequencies for each structure.

Table 2.1: Simulation parameters and peak wavelength values for Prototypes 1-3

Simulation	Radius (nm)	Depth (nm)	Meas. λ_{peak} (nm)	Sim. λ_{peak} (nm)	Delta
Prot. 1	450	560	1220	1280	+4.69%
Prot. 2	440	315	980	1020	+3.92%
Prot. 3	390	600	1260	1350	+6.67%

In general, there is good agreement between the measured and simulated results. The resonant peaks are within 6.7% of the predicted value, and the long-wavelength behavior (> 3 μm) approaches simulation. The discrepancies between simulations and measurements are now examined in terms of the prototypes' resonant cavity quality factor.

Looking at Figs. 2.9, 2.11, and 2.13 one observes that the resonant peaks are sharper and narrower on the simulation curves than on the measurement curves. The tall, narrow resonant peaks are an indication of high resonant cavity quality factor. The measured resonant peaks are not as sharp as the simulated ones, therefore pointing to losses that have not been included in the simulation. There are two loss mechanisms in our case: structural and material. Table 2.2 summarizes the dominant differences between the simulated structures and the actual prototypes.

Diameter variability causes the structure to have several different resonant peaks. The effect of a single diameter across the entire sample is a single resonant frequency, while the cumulative effect of various resonant frequencies broadens and lowers the peak intensity. The worst-case diameter variability in these prototypes is 6.7%, and 2.4% in the best. From the measurements of prototype behavior we see that the influence on selective radiation properties is not devastating. The diameter variability across the sample area stems from the fabrication process, specifically the lithographic exposure and hard-mask etching steps. The nature of the lithographic exposure system is such that some variation in diameter is inevitable when large areas of sample are exposed. Our samples require some of the largest areas exposed using this particular lithography system. The hard-mask etching step is a wet chemical etch of poly-crystalline chromium. Wet chemical etches are highly unpredictable compared to dry etching techniques. Another member of our laboratory is already investigating dry-etching options for the chromium hard-mask that are expected to resolve this issue.

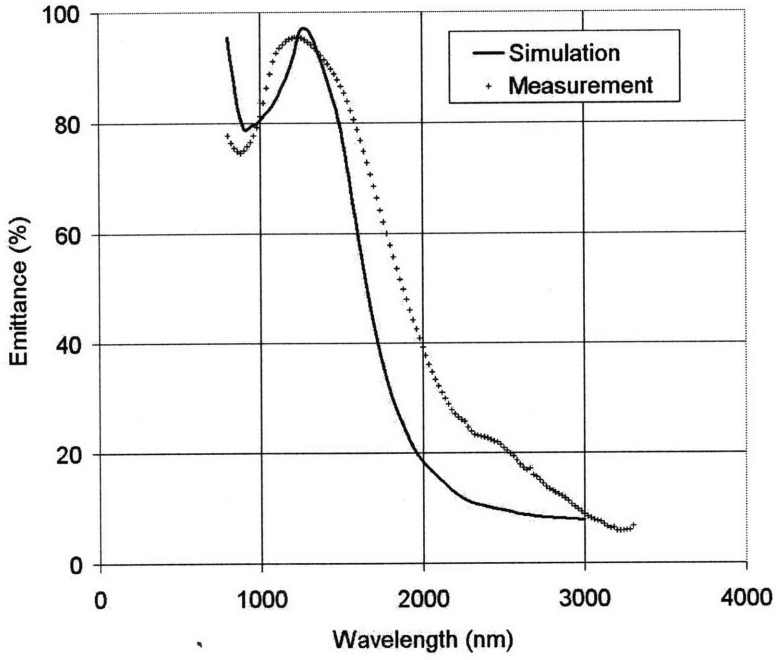

Figure 2.9: Measured and simulated normal emittance for Prototype 1

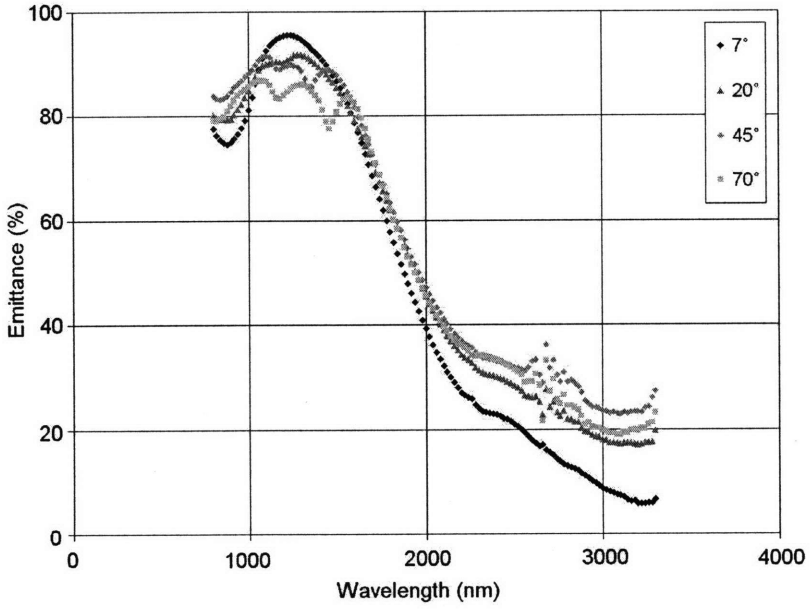

Figure 2.10: Prototype 1 measured emittance for several angles

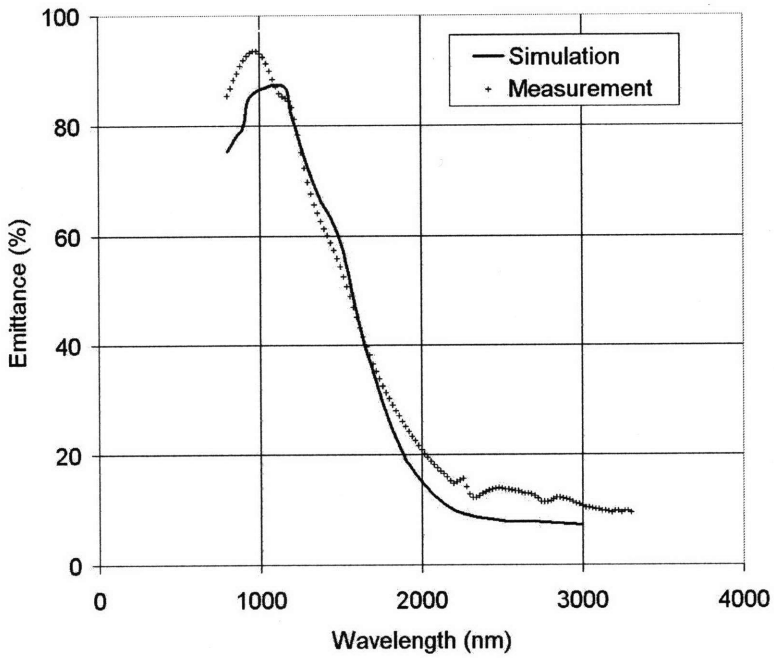

Figure 2.11: Measured and simulated normal emittance for Prototype 2

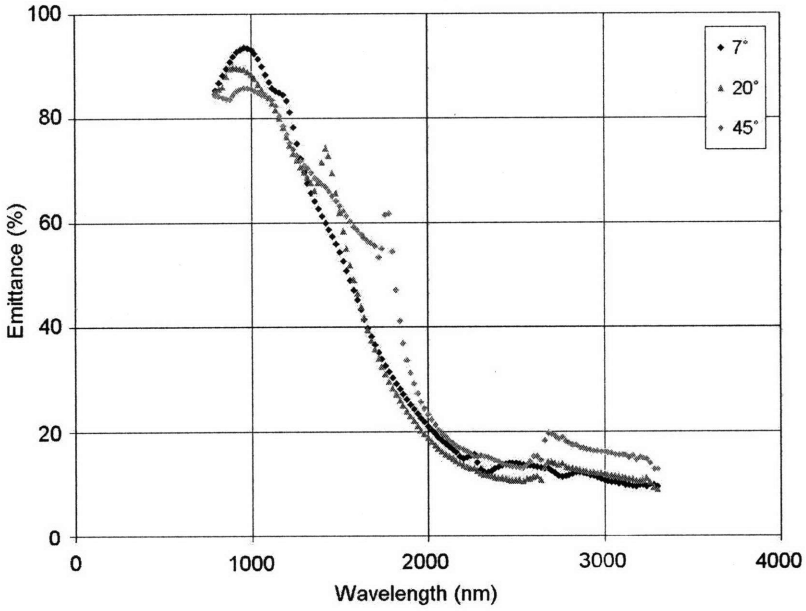

Figure 2.12: Prototype 2 measured emittance for several angles

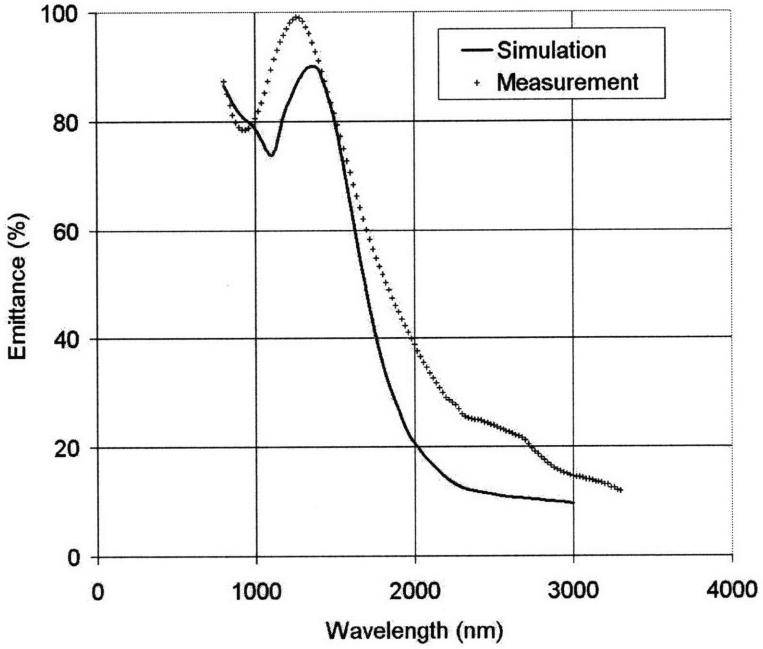

Figure 2.13: Measured and simulated normal emittance for Prototype 3

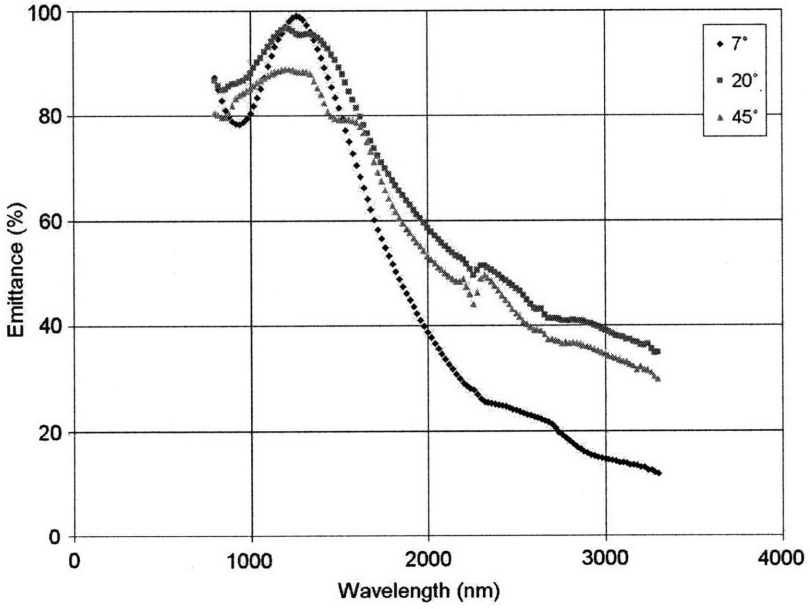

Figure 2.14: Prototype 3 measured emittance for several angles

Table 2.2: Additional loss mechanisms, not included in current simulations

Loss	Prototype 1	Prototype 2	Prototype 3
Structural			
Diameter variability	6.7%	5.3%	2.4%
Wall slant	0.05	0.09	0.04
Surface roughness (max)	100nm	40nm	20nm
Material			
Refractive index *	3.7%	3.7%	3.7%
	* *Maximum absolute difference from reference index values.*		

Wall slant (ratio of lateral and vertical wall displacement) also has its roots in the fabrication process, and can also cause various resonant frequencies due to its influence on the effective cavity diameter. The cause of non-zero wall slant in our case is the lateral erosion of the chromium hard-mask during the tungsten reactive ion etch. In turn, the lateral erosion is caused by the non-zero aspect ratio of walls in the hard-mask itself. As with diameter variability, we expect that the issue of slanted walls in the hard-mask will be resolved by using a dry etching technique.

At this time, nanoscale electromagnetic phenomena are not fully understood. It can be said that all deviations from the simulated structure, including random rough features as small as 10 or 20 nm, will result in some losses compared to the ideal simulated behavior. From our results it is evident that these small features do not overwhelm the primary mechanism of radiation. Extensive simulations could more precisely answer the question of influence of small rough features on the overall radiation spectrum. Surface roughness results from the tungsten reactive ion etch step. During that etch step the tungsten, and the chromium hard-mask covering it, are exposed to prolonged bombardment with high-energy ions. Although the primary mechanism in the tungsten etch is that of chemical reactions, there is also a mechanical process that gradually introduces faults in the chromium mask. If these faults punch through the entire thickness of the chromium mask, then the underlying tungsten will be exposed and begin to etch. A thicker chromium mask would resolve the surface roughness issue. However, at the time of this work, the available chromium deposition equipment (used for a variety of materials) was limited as to how much chromium can be deposited. A dedicated chromium deposition machine would not encounter this problem.

The material issues stem from the substrate quality and are exacerbated during fabrication. The emitter behavior hinges on the optical properties of the material from which it is made; any deviations in optical properties of the substrate material manifest themselves in the emitter behavior. The relationship between the material properties and the emitter behavior is highly non-linear and the influence of even the small changes in optical prop-

erties is difficult to predict without extensive additional simulations. Figure 2.7 shows the flat tungsten emittance based on reference refractive index values and a measurement of one of the wafers used to produce our prototypes. All simulations in this research were performed using the reference values. Clearly, the difference between the reference and the measured refractive index properties is the main cause of increased emittance of our prototypes for wavelengths above 1.5 μm. In addition to differences in raw material, prolonged exposure to the tungsten reactive ion etch (over 90 minutes) also deteriorates the material properties. Some of the high-energy ions bombarding the chromium mask travel deep into the chromium mask and the underlying tungsten resulting in disturbances of the tungsten's crystalline structure near the tungsten surface. For example, prototype 2 (Fig. 2.11) is the shallowest and has undergone the shortest tungsten etching process, leading to less material disruption and better agreement between simulation and measurement at longer wavelengths. From previous investigations, we have seen that amorphous tungsten has higher emittance for long wavelengths than crystalline tungsten [43], which is in line with the performance of our prototypes.

Angled emittance measurements (Figs. 2.10, 2.12, and 2.14) show that the prototypes generally preserve their selective emittance behavior for a wide angle of incidence. Atmospheric interference due to VASRA architecture is evident in the 2.5-3 μm wavelength range, as expected.

Clearly, interesting investigations could be performed to understand each of the loss mechanisms in more detail. An iterative approach of alternating simulation and fabrication refinements would eventually lead to the deepest understanding of these structures. An expanded list of suggestions for future research can be found in Section 4.2.

2.4.3 Spectral Efficiency

An important indicator of selective emitter performance is its spectral efficiency (Sec. 1.1.3). Spectral performance of the selective emitter prototypes is shown in Figs. 2.15, 2.17, and 2.19. Figures 2.16, 2.18, and 2.20 show how the black-body spectrum is affected by the three selective emitter prototypes coupled with our previously-produced dielectric stack mirror experimental results [10]. The curves in these figures are based on black-body calculations (according to Planck's Law) and the measured room-temperature properties of the dielectric stack mirror and the selective emitter prototypes.

The dielectric stack mirror contributes to system efficiency by reflecting any photons that cannot be converted into free charge carriers. For wavelengths above 1.8 μm the mirror reflects nearly all photons back to the selective emitter where these photons are recycled and re-emitted. Therefore, in addition to keeping the PV cell cool and efficient, the dielectric stack mirror is also a fuel-saving component of the system.

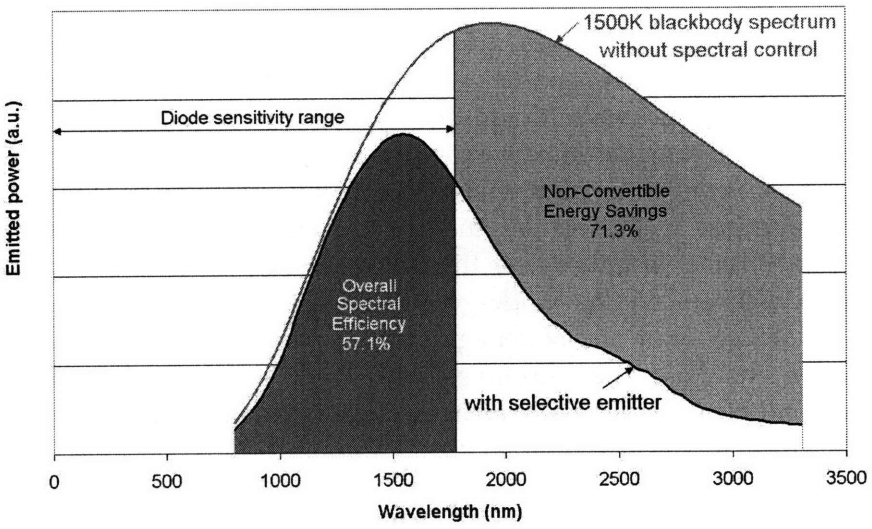

Figure 2.15: Prototype 1: Comparison of energy delivered by black-body and by the selective emitter

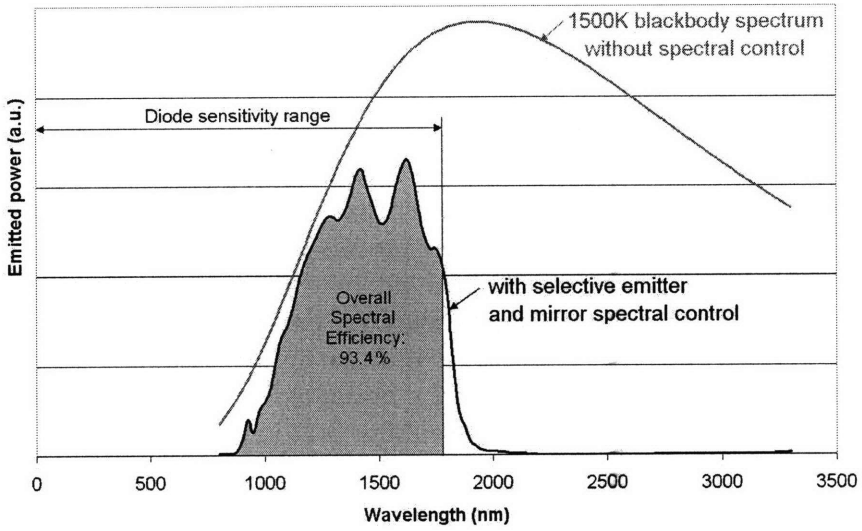

Figure 2.16: Prototype 1: Comparison of energy delivered by black-body and by a combination of black-body, selective emitter, and dielectric stack mirror

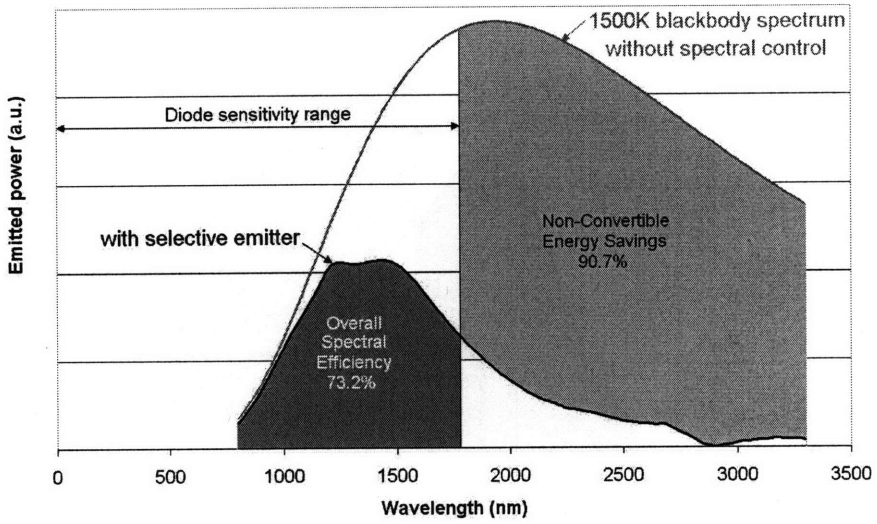

Figure 2.17: Prototype 2: Comparison of energy delivered by black-body and by the selective emitter

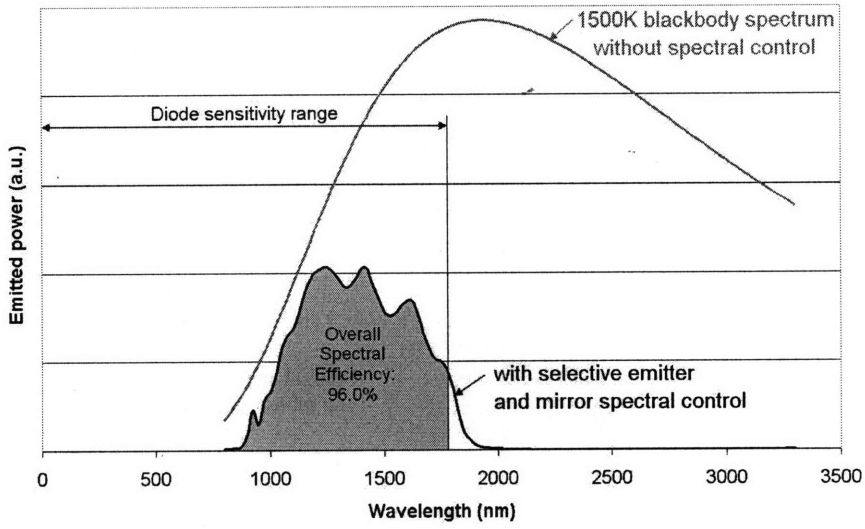

Figure 2.18: Prototype 2: Comparison of energy delivered by black-body and by a combination of black-body, selective emitter, and dielectric stack mirror

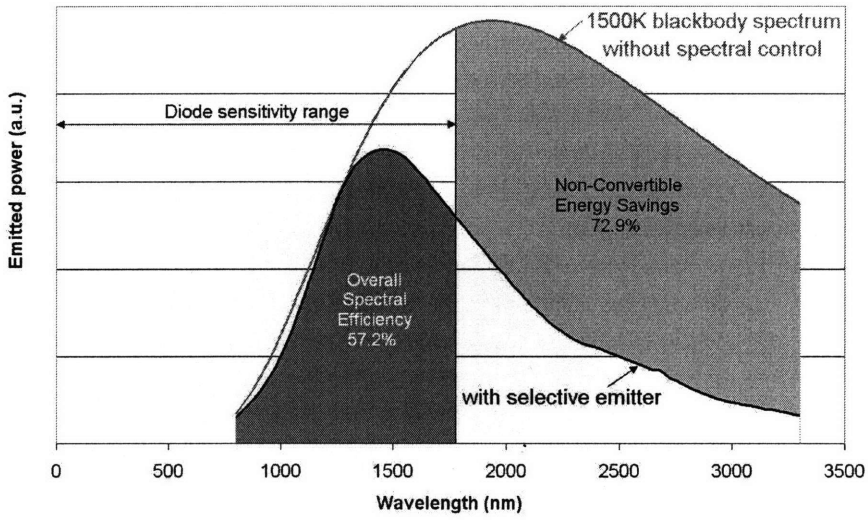

Figure 2.19: Prototype 3: Comparison of energy delivered by black-body and by the selective emitter

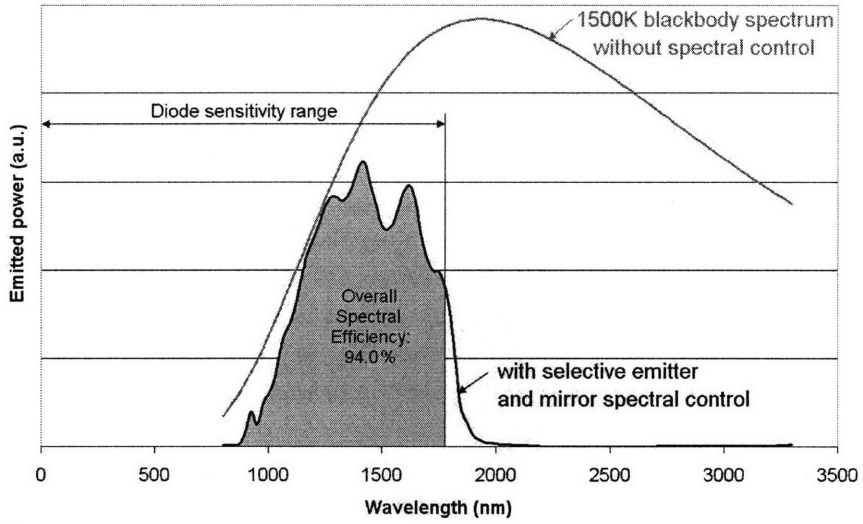

Figure 2.20: Prototype 3: Comparison of energy delivered by black-body and by a combination of black-body, selective emitter, and dielectric stack mirror

Spectral performance parameters for all three prototypes are given in Table 2.3. The first column refers to the spectral efficiency (η_{cS}) of the emitter-mirror combination. The combination's spectral efficiency is defined as the ratio of energy incident upon the diode below the band-gap wavelength (λ_g) to the total energy delivered to the diode.

Although prototype 2 has the highest spectral efficiency, the prototype design is not necessarily the best selective emitter for all TPV applications. The TPV system efficiency depends on the amount of energy provided by the selective emitter compared to a black-body at the same temperature (power density). The second column of Table 2.3 lists the power density for each prototype compared to a black-body. In-band energy efficiency is defined as the ratio of spectrally-controlled energy below λ_g and black-body energy below λ_g.

In addition, Table 2.4 contains the efficiency parameters of each prototype without the influence of the dielectric stack mirror. Prototype 2 provides just about half of the otherwise available black-body energy (56.4%), while prototypes 1 and 3 provide over 80%.

From the last column of Table 2.4, it is evident that all three prototypes are very efficient at suppressing radiation that is outside the diode's conversion range. This is extremely important as all the savings in the non-convertible range translate directly to fuel savings. Therefore, compared to black-body, all three emitter prototypes provide for drastically lower fuel consumption and gaseous emissions.

Table 2.3: Combined spectral efficiencies of the dielectric stack mirror and selective emitter prototypes based on room-temperature measurements and extrapolated to 1500 K black-body radiation

Prototype	η_{cS} [1]	η_{cP} [2]	η_{cNCS} [3]
1	93.4%	71.0%	97.8%
2	96.0%	46.6%	99.1%
3	94.1%	67.7%	98.1%

(1) *Spectral efficiency: Ratio of energy below λ_g and total energy delivered to the diode*

(2) *Power density: Ratio of spectrally-controlled energy below λ_g and black-body energy below λ_g*

(3) *Non-convertible energy savings: efficiency at suppressing non-convertible energy*

2.5 High-Temperature Spectral Characterization

High-temperature emission properties of the fabricated prototypes were measured using a Nicolet Magna 860 Fourier transform infra-red (FTIR) spectrometer (at the MIT Center for Materials Science and Engineering). The results of high-temperature measurements

Table 2.4: Spectral efficiencies of the selective emitter prototypes based on room-temperature measurements and extrapolated to 1500 K black-body radiation (without the dielectric stack mirror)

Prototype	η_{eS} [1]	η_{eP} [2]	η_{eNCS} [3]
1	57.1%	84.7%	71.3%
2	73.2%	56.4%	90.7%
3	57.2%	80.6%	72.9%

(1) *Emitter spectral efficiency: Ratio of energy below λ_g and total energy delivered to the diode*

(2) *Emitter power density: Ratio of spectrally-controlled energy and black-body energy below λ_g*

(3) *Emitter non-convertible energy savings: efficiency at suppressing non-convertible energy*

provided us important insights into the durability, vacuum requirements, and radiated power of our selective emitters.

The basic components of an FTIR are the detector, the beamsplitter, and a series of flat and parabolic mirrors routing the signal from the source to the detector. For high-temperature emission measurements (Fig. 2.21) the sample is coupled to the FTIR external port. In our case, the sample was affixed onto a heater using a custom-made mount, and the heater-sample assembly placed inside a vacuum chamber. The vacuum is necessitated by tungsten's strong reactivity with oxygen at elevated temperatures. Maintaining a vacuum of 10^{-4} - 10^{-5} Torr has been sufficient to prevent tungsten oxidation.

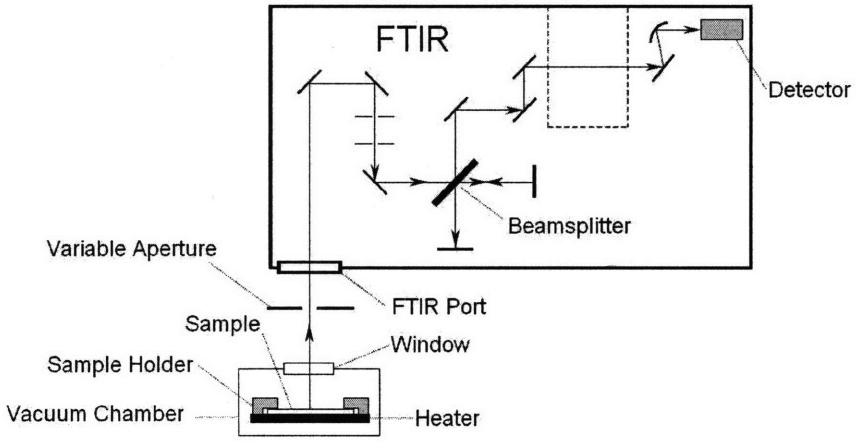

Figure 2.21: Basic assembly for FTIR high-temperature emission measurement (not to scale)

The heater used in these measurements was a General Electric boron-nitride ceramic heater capable of temperatures up to 1100°C. The heater was mounted to a stand using two long screws and placed inside the vacuum chamber (Fig. 2.22). The two shorter screws pointing

up were used to affix the sample holder. A photograph of a mounted sample (with sample holder) and vacuum chamber port is shown in Fig. 2.23. The sample is visible through the round hole in the center of the image. The heater, sample and sample holder are all placed inside a specially-designed vacuum chamber and connected to the thermocouple and electrical supply leads (Fig. 2.24).

Several rounds of FTIR measurements were conducted for flat tungsten and selective emitters using mercury-cadmium-telluride (MCT) and indium-antimonide (InSb) detectors. Results for flat tungsten and a tungsten selective emitter (prototype 1) are shown in Fig. 2.25 and 2.26, respectively. The temperatures were determined by thermocouple measurements and regression analysis of black-body and measured curve ratios. The valid detector range for these measurements was 1.5-5.2 μm. Absorption peaks are clearly visible around 1.9 (H_2O), 2.7 (H_2O), 3.4 (CH_4), and 4.26 μm (CO_2), and are due to the large atmospheric length of the beampath.

The prototype 1 measurement at 1100°C (1373 K) was compared to the room-temperature measurement for the same prototype scaled by the black-body radiated power at 1100°C (Fig. 2.27). Significant deviation from expected values is seen for wavelengths longer than 1600 nm. The optical properties of tungsten change drastically with temperature [44]. A comparison of flat tungsten emittance at room-temperature [12] and 1500 K [44] is shown in Fig. 2.28. The change in the optical properties of tungsten is the main cause for the large difference between the measured high-temperature selective emitter behavior and the expected performance based on room-temperature measurements and black-body simulations.

The precision of the FTIR measurements is challenged by the FTIR system itself, its non-linear, time-variant detectors, and changes in tungsten's optical properties with temperature. The intended use of the FTIR system is to compare a sample measurement to a 100% baseline such as full transmittance or reflectance. In our case, there was no possibility of 100% emission baseline, as we did not have access to a perfect black-body radiation source. Also, the detectors used in the FTIR had limited wavelength range and highly-varying response. Despite these FTIR challenges, one very useful result lies in the ratio of radiation of selective emitter and the flat tungsten.

The ratio of the selective emitter prototype 1 and flat tungsten radiation at 1100°C and the ratio of selective emitter prototype 1 and flat tungsten emittance at room temperature (both measured and simulated) are show in Fig. 2.29. The two ratios don't match precisely, which can be expected considering the differences in detection technologies and temperatures. It can be observed, however, that the ratios are on the same order of magnitude, which is highly encouraging.

Of the three prototypes, only prototype 1 high-temperature emissions measurements were successful. During the prototype 3 measurements, a vacuum failure occurred while the sample was at high-temperature. This has resulted in sample oxidation, and the emitter

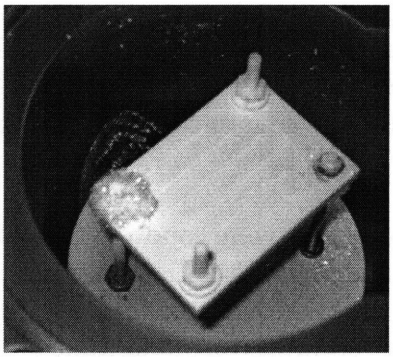

Figure 2.22: Ceramic heater mounted to a stand, as viewed from the vacuum chamber port.

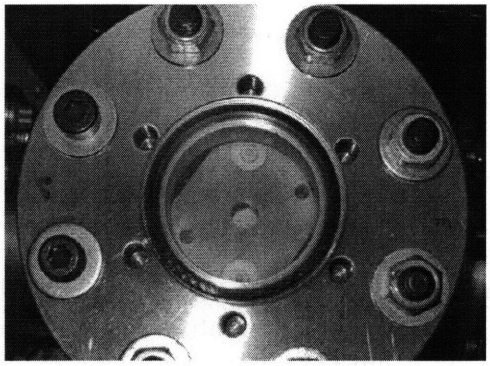

Figure 2.23: Sample and sample holder as seen through the window of the vacuum chamber.

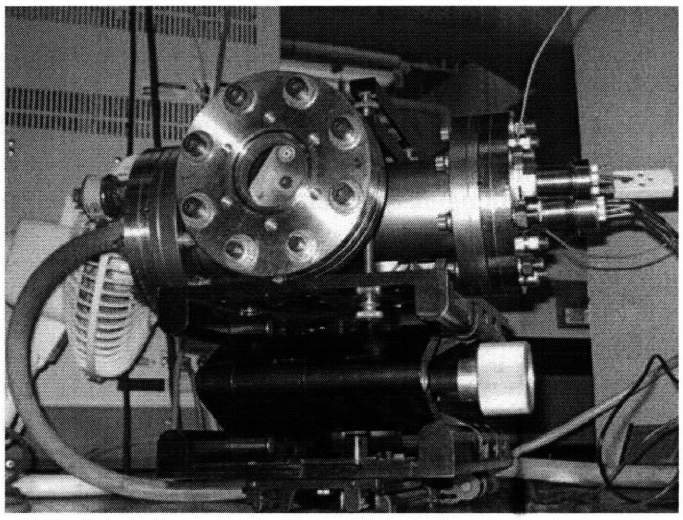

Figure 2.24: Full FTIR emissions assembly, with vacuum hose and gauge visible on the left, and the temperature control and electrical supply leads on the right. The chamber is mounted on a three-axis adjustable stand.

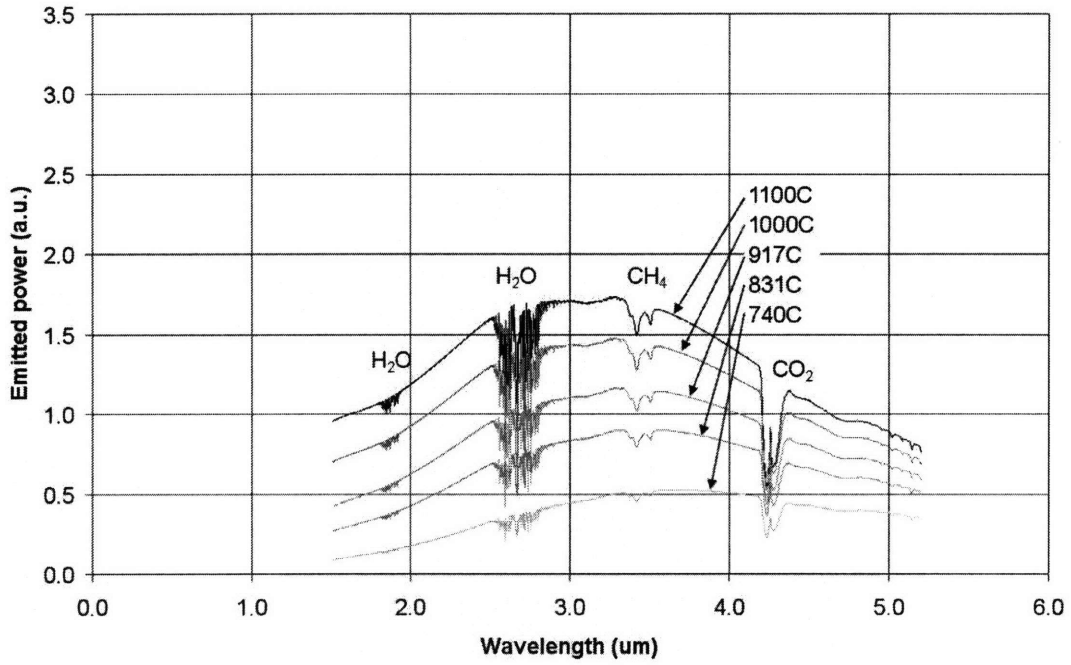

Figure 2.25: Flat tungsten high-temperature FTIR emission measurement for several temperatures

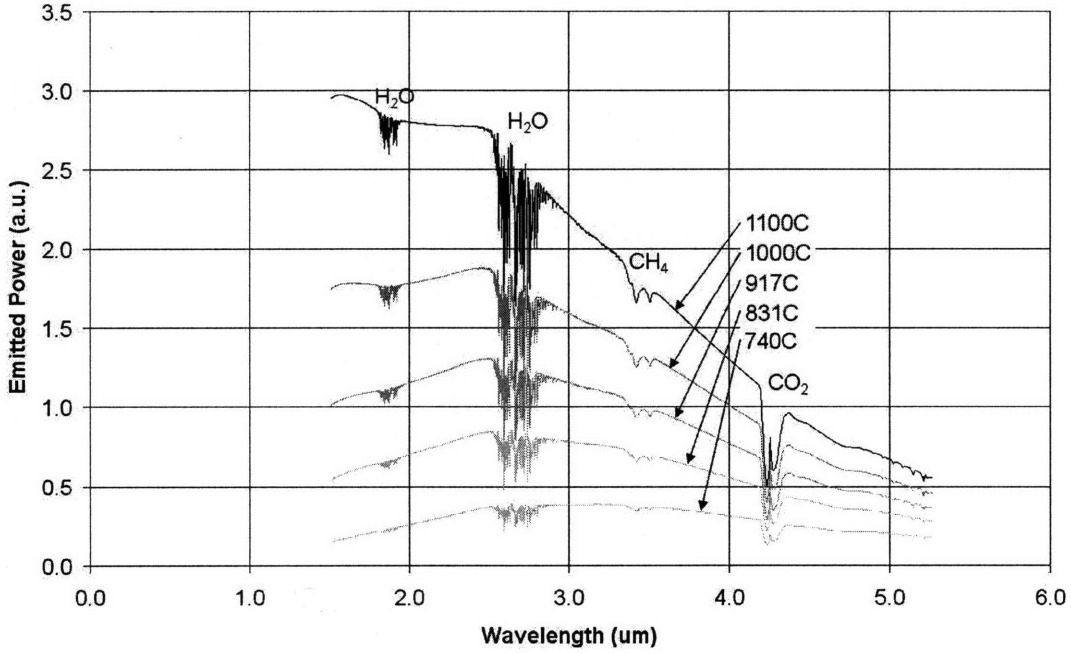

Figure 2.26: Tungsten selective emitter (Prototype 1) high-temperature FTIR emission measurement for several temperatures

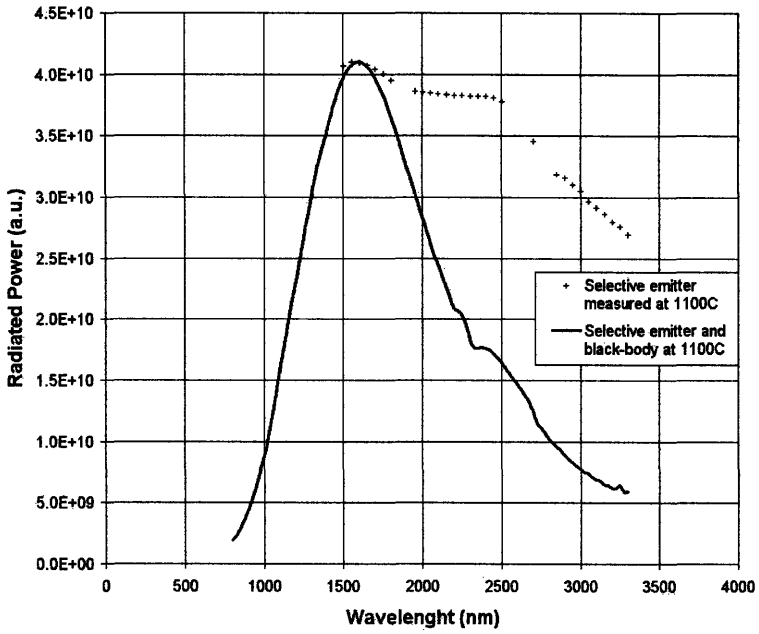

Figure 2.27: Tungsten selective emitter (Prototype 1) FTIR emission measurement at 1100°C and prototype 1 room-temperature measurement coupled into black-body radiation at 1100°C

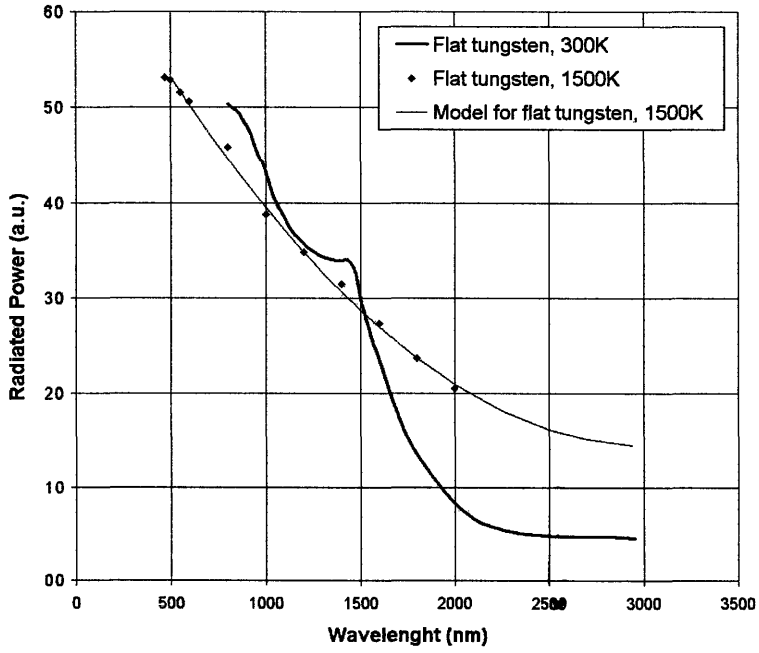

Figure 2.28: Flat tungsten emittance at room-temperature [12] and 1500K [44]

pattern was severely damaged. Figure 2.30 shows the influence of oxygen atmosphere on our nano-scale selective emitter pattern. Prototype 2 remains intact after several hours of high-temperature exposure in 10^{-4} Torr vacuum. However, the heater used for the high-temperature measurements has failed due to material fatigue during the most recent attempted measurement.

Based on results shown in Fig. 2.26, the selective emitter radiates three times more powerfully than flat tungsten at 1.7 μm. Due to heater limitations, the highest temperature for this particular measurement was about 1375 K, which is 125 K lower than the target temperature for our TPV system. Following Planck's law, an increase in temperature would shift the radiation spectrum towards shorter wavelengths. The peak of black-body radiation shifts from 2.2 μm at 1300 K, to 1.9 μm at 1500 K (Fig. 1.2). Therefore, at 1500K we can expect a radiation spectrum even more suitable for GaSb PV cells with the cut-off wavelength of 1.77 μm.

2.6 Summary

This chapter has addressed the design, simulation, and optical characterization of selective emitter prototypes for TPV applications. We have examined the effect of cavities and planar surface on the overall behavior of a selective emitter. Poly-crystalline tungsten foil has been studied as a cost-efficient alternative to single-crystal tungsten wafers. Second-pass simulations for each prototype have shown excellent agreement with measurements. Coupling of the measured selective emitter and dielectric stack mirror properties with simulated black-body radiation yielded as much as 96% overall spectral efficiency, which is as much as 11% more than efficiencies reported in literature [8, 37]. Furthermore, our spectral control method has potential for excellent fuel savings by blocking 99% of non-convertible energy. Selective emitter high-temperature measurements show as much as 3X radiative improvement over flat tungsten. All measurements indicate that our selective emitter and dielectric stack mirror designs will dramatically boost TPV system efficiencies.

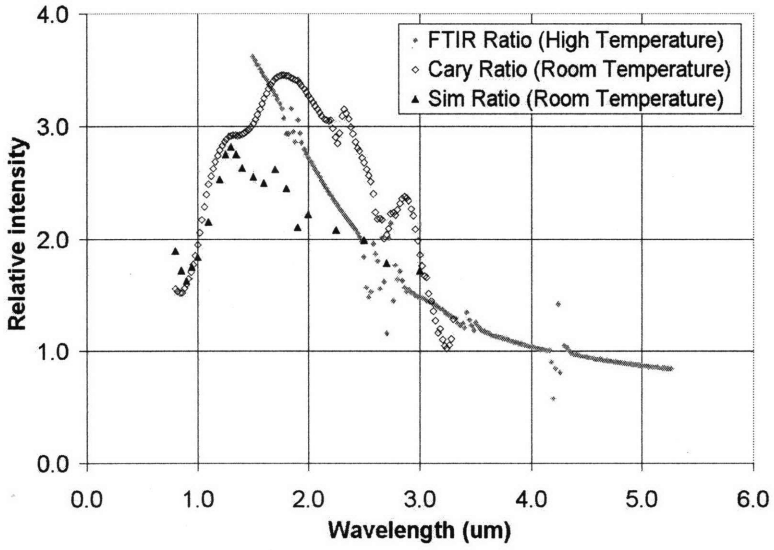

Figure 2.29: Prototype 1 ratios of selective emitter and flat tungsten measurements at 1100°C (measured by FTIR), room temperature (measured by Cary spectrophotometer), and room temperature simulations

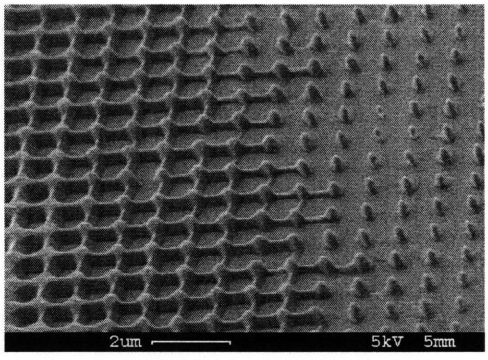

Figure 2.30: Prototype 3 after oxidation damage at high-temperature

Chapter 3

Fabrication Methods

The 2D PhC fabrication process consists of two major parts: lithography and etching. Both processes are scalable, fast, inexpensive, and versatile. Wherever possible, standard microfabrication materials and techniques were used. Our etching process can be used identically from case to case for pattern dimensions of similar orders of magnitude. The lithography process is applicable to a variety of structures with only minor modifications. The following sections present the materials, processes, and parameters used in the fabrication of 2D PhC samples.

3.1 Process Flow

The fabrication process steps are presented in Fig. 3.1 and illustrated in Fig. 3.2. Clean sample surface is crucial to the success of the fabrication process. The fabrication process, therefore, starts with assuring that the sample is free of physical contaminants. An alcohol rinse and nitrogen dry were found sufficient to provide a clean sample surface on wafers arriving directly from the manufacturer.

The chromium (Cr) "hard-mask" layer is deposited using electron-beam evaporation. The chromium layer quality greatly influences the precision of the final structure. Care must be taken to deposit the chromium layer under optimal conditions. This includes allowing for good vacuum (less than 10^{-5} Torr) and thoroughly cleaning the deposition chamber. More discussion on the quality of the chromium layer and its influence on performance will be provided in Section 3.3.3.

The two lithography layers - anti-reflective coating (ARC) and photoresist (PR) - are applied using a spinning stage. The ARC used in this process is cyclohexanone-based BARLi® by AZ Photoresist Products, Hoechst Celanese Corporation; the photoresist used is THMR-iNPS4® by OHKA America (PS-4). After lithographic exposure the process is subtractive: the desired pattern is transferred from the one layer to the next by various etching processes. The following sections will offer method parameters, descriptions, and calibration techniques.

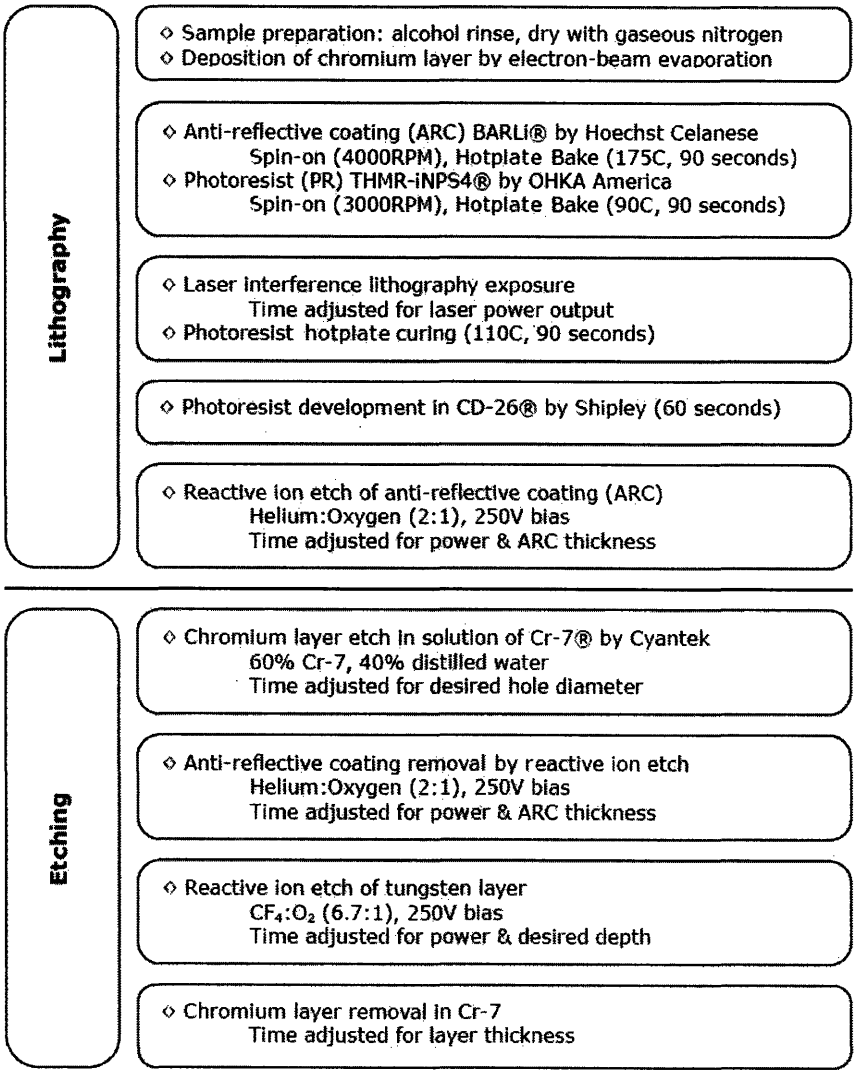

Figure 3.1: Fabrication process steps

3.1.1 A Note on Calibration Procedures

Each step of this fabrication process has undergone strict calibration procedures. These procedures had two purposes: (1) to determine the operating range of our chemicals and equipment; and (2) to determine optimal parameters for our particular prototype dimensions. Ideally, the calibration procedures would be conducted on the same substrate as used for the final version of the prototype. However, tungsten substrates are (at the time of this thesis) quite expensive, and their use for calibration experiments would be financially imprudent.

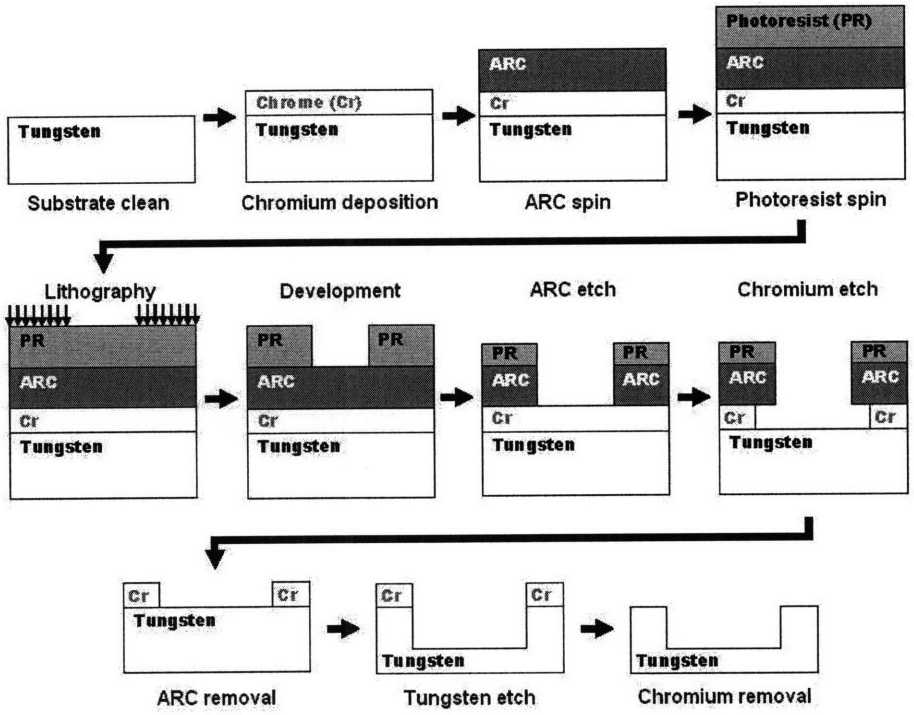

Figure 3.2: Fabrication process flow

Instead, a large number of calibration procedures were conducted on a "pseudo-tungsten" substrate. The pseudo-tungsten substrate consists of a silicon wafer coated with a thin layer of tungsten (deposited by electron beam evaporation). These pseudo-tungsten substrates are much less expensive, yet just as useful for calibration procedures. Specifically, all lithography, ARC etch, and chromium etch calibrations were conducted on pseudo-tungsten substrates. Only the tungsten etch experiments were conducted on actual tungsten substrates.

3.2 Lithography

Laser interference lithography is a relatively inexpensive, but extremely effective, fast, and precise lithography technique. A wide variety of patterns can be created using relatively simple equipment. A single-wavelength light-source can create a range of patterns and periods that exceed the capabilities of much more complicated stepper systems [45]. Laser interference lithography systems are much faster than stepper systems and scanning electron beam lithography systems, exhibit better pattern coherence across large areas of exposure, and can achieve comparable resolution.

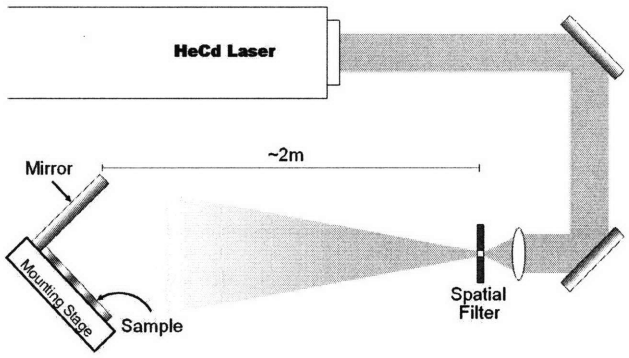

Figure 3.3: Schematic of the Lloyd's mirror laser interference lithography equipment set-up

As the name implies, the principle behind the laser interference lithography technique is that of interference of two coherent light beams. The laser interference lithography work described here was carried out using the Lloyd's mirror interferometer at the MIT Nano-Structures Laboratory (NSL). The interferometer is named after Humphry Lloyd, who proposed the method in 1837 [46]. The system, illustrated in Fig. 3.3, uses a helium-cadmium (HeCd) laser emitting at 325 nm. The relatively long (2 m) separation between the source and the sample is required in order to achieve an approximate plane wave incidence at sample surface.

Instead of having two sources of light, the Lloyd's mirror system makes use of a mirror to provide the second interfering light-wave. Figure 3.4 illustrates how the incident wave and the wave reflected from the mirror form the interference pattern on the substrate. Depending on the size of the mirror and the incident angle, an area of the sample may remain unexposed (see right end of sample in Fig. 3.4).

The physics behind laser interference lithography is relatively simple. In Fig. 3.5, $\mathbf{E}_1$ and $\mathbf{E}_2$ are sinusoidally-dependent electric field vectors with magnitudes E_1 and E_2 in the **y** direction, incident at angle θ from the normal to the sample surface. The incident waves can be decomposed into horizontal and vertical components (Fig. 3.6). Interference of the horizontal components of such waves forms a standing wave pattern of gratings on the sample surface — alternating regions of illumination — that can be captured using light-sensitive chemicals (photoresists). The period, P, of the interference grating can be found using the distribution of intensity method [47]. The period of the grating, P, is dependent on the light's wavelength (λ) and the angle at which the wave's intersect (θ), as given by:

$$P = \frac{\lambda}{2\sin\theta} \tag{3.1}$$

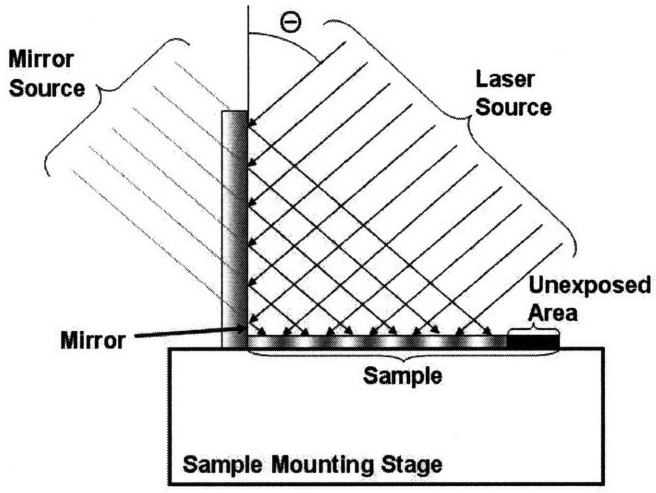

Figure 3.4: Incident and reflected wave interference in a Lloyd's mirror system

Laser interference lithography allows for a variety of shapes and periods to be formed through the use of multiple light waves and multiple exposures, with the same or varying doses and periods [45]. Even though laser interference lithography is limited to only periodic structures, it has found broad use in technology as periodic structures have a variety of applications.

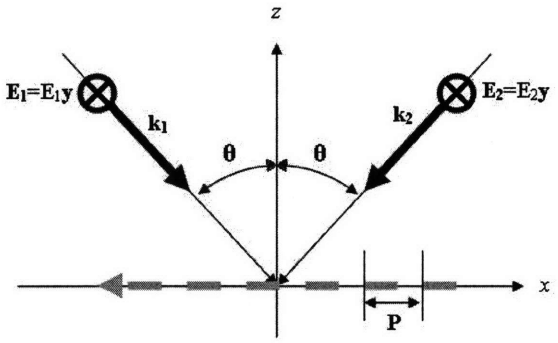

Figure 3.5: Interference of two TE waves incident at angle θ forming a pattern on the $x-y$ plane

To create a two-dimensional pattern, the sample is exposed twice (Fig. 3.7). Between the two exposures the sample is rotated by 90^o in the plane of the sample holder. For this process, the exposures are carried out at the same incident angle and for the same amount of time. The same incident angle results in the same periodicity of the two exposures. The same amount of time for each exposure results in the same duty cycle of the gratings.

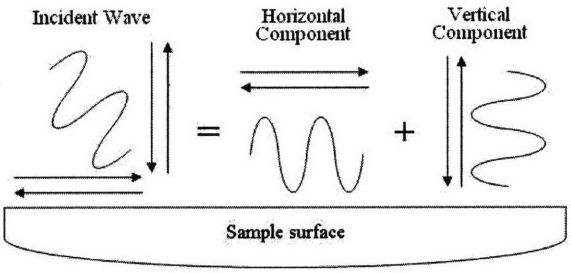

Figure 3.6: Decomposition of an incident sinusoidal wave into the horizontal (desired) and vertical (undesired) components

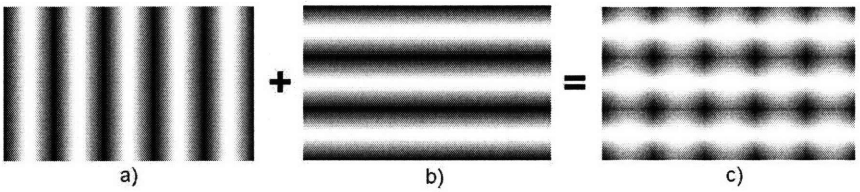

Figure 3.7: Exposure process: a) first lithography exposure; b) second lithography exposure at 90^o from the first; c) resulting lithographic pattern.

The shape of the hole—it's "roundness"—is established during the lithographic exposure. The "proximity effect," commonly seen in lithographic exposures in which the period of the structure approaches the wavelength of the exposing light, is responsible for the square shape of the holes at shorter exposure times (Fig. 3.8). Testing was performed to determine appropriate exposure times for the desired hole shape. These calibration tests also established a baseline for photoresist sensitivity and laser power fluctuations. For a square pattern, the minimum exposure required to obtain a pattern was 35 seconds at a laser power of 170 μW in the plane of the sample.

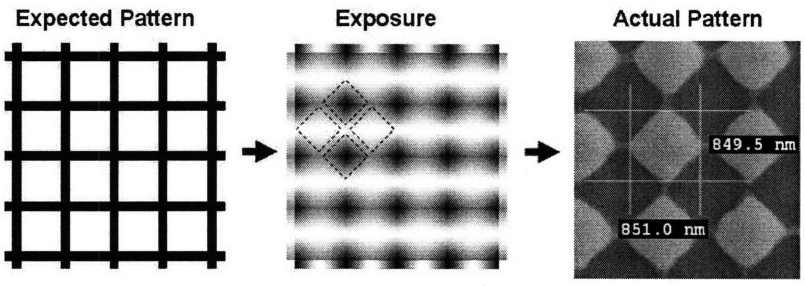

Figure 3.8: Proximity effect is observable when the feature size approaches resolution limits. The shape of each feature is influenced by its distance from other features.

The scanning electron micrographs (SEMs) of the developed patterns in photoresist for a variety of exposure times (at a laser power of 170 μW) are shown in Fig. 3.9. For the times of interest, the relationship between the exposure time and the pitch of the structure, defined

as the ratio of hole diameter to the structure period, is approximately linear. Although the exposure time can be used to determine the hole radius, in our case the final radius is determined by the lateral progress of the chromium etch. Therefore, in the lithography step, the main objective is to achieve a circular hole shape.

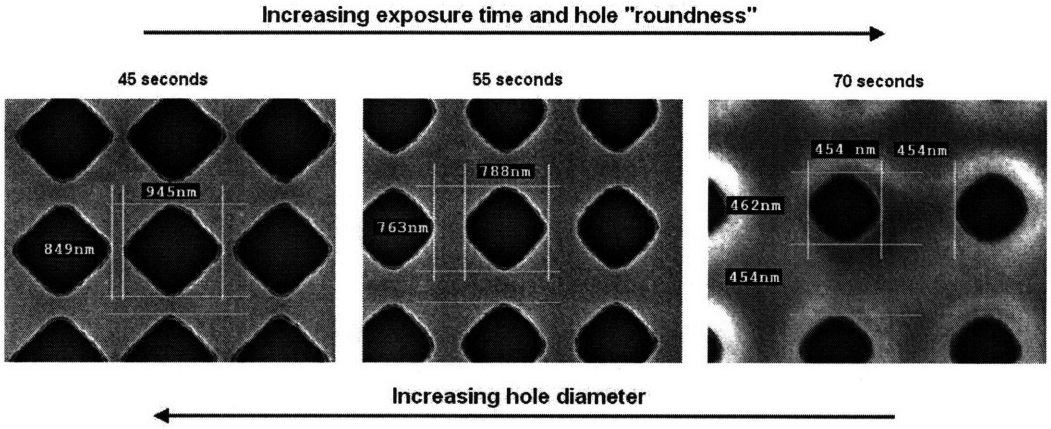

Figure 3.9: Relationship of the hole diameter, roundness, wall thickness, and exposure time, for a laser power of 170 μW.

The desired structure in this process is a square array of large round holes separated by thin walls. Considering the dimensions required in the selective emitter design using laser interference lithography limits us to either round holes with thick walls, or square holes with thin walls (Fig. 3.9). At this point in the process flow it is not possible to satisfy both structure requirements. This problem is solved during the hard-mask wet etch, which is used to widen the holes to the desired diameter, while preserving their round shape. More details on the hole-widening approach will be provided in Sec. 3.3.

Light interference is at the core of our lithography process, but it also presents a pattern precision challenge. Recall that the incident wave can be decomposed into a horizontal and a vertical component (Fig. 3.6). Just like the interference of the horizontal components results in the horizontal patterning of the resist, so does the interference of the vertical components result in the vertical patterning of the photoresist walls. In the vertical case, the reflected component comes from the hard-mask surface (Fig. 3.10).

Recall the vertical component from Fig. 3.6. The vertical standing wave, if powerful enough, will result in vertically sinusoidal walls within the photoresist layer. The anti-reflection coating (ARC) is used to minimize the effect of the vertical standing wave on the lithographic pattern. A comparison of lithography results with and without an ARC layer is given in Fig. 3.11. Strong vertical "scalloping" is evident in the sample fabricated without the ARC layer. This vertical patterning is not desirable because it deteriorates the resolution of the pattern. To reduce the influence of the vertical patterning, the ARC layer is placed between the photoresist and the substrate in order to minimize the power of the

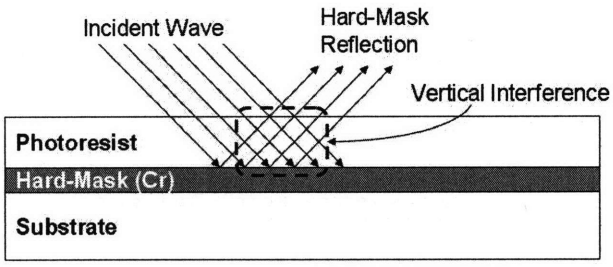

Figure 3.10: Vertical interference resulting from reflective hard-mask surface

vertical standing wave (by minimizing the power of the reflected vertical component) and enable fabrication of straight sidewalls in the photoresist.

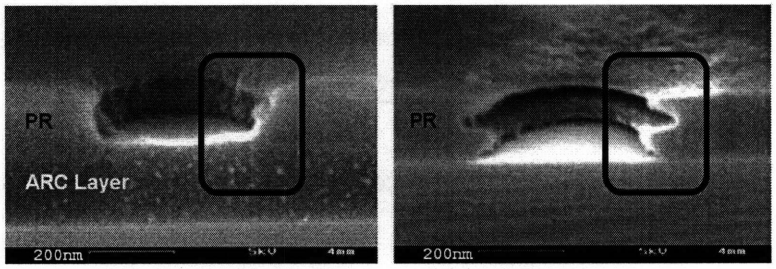

Figure 3.11: Scanning electron micrographs (SEMs) showing exposure results in photoresist (PR) with an ARC layer (left) and without an ARC layer (right)

To apply liquid photoresist or ARC, the substrate is placed on a spinning stage, the liquid is dripped onto the wafer forming a puddle, and the stage is spun. Centrifugal forces distribute the photoresist material onto the substrate surface. The relationship between the spinning rate of the stage and the resulting thickness of the layer for photoresist and ARC ("spin curves") are shown in Figs. 3.12 and 3.13. Layer thicknesses were measured using an ellipsometer. Spin curves are a part of photoresist and ARC calibration, and should be repeated whenever a new batch of the chemicals is used. The "optimal operating range" for a spun liquid is the flatter portion of the spin curve. This ensures minimum dependence on rpm variations. PS-4 and BARLi should not be applied at rotation rates less than 3000 rpm.

A simulation is used to determine the minimum reflectance and the appropriate thicknesses for the photoresist and the ARC layers [45]. The results of the reflectance simulation are shown in Fig. 3.14. The parameters of the simulation are given in Table 3.1. Initial simulation determined that the photoresist thickness does not affect the reflectance at the ARC-hardmask interface. Therefore, a convenient thickness of 210 nm (applied at 3000 rpm) was chosen for the ARC layer.

The minimum reflectance from the interface between the chromium and the ARC layers for the transverse electric (TE) and the transverse magnetic (TM) mode occurred at 242 nm

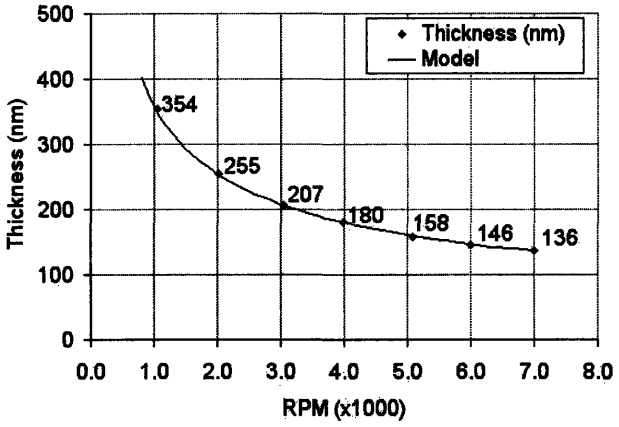

Figure 3.12: The PS4 photoresist layer thickness as a function of constant rpm for 60 seconds of spinning.

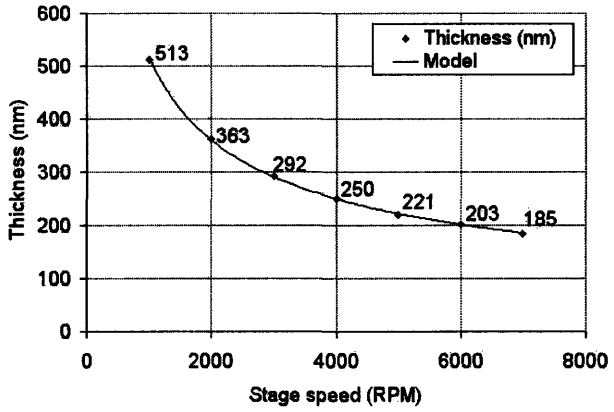

Figure 3.13: The BARLi ARC layer thickness as a function of constant rpm for 60 seconds of spinning.

and 250 nm, respectively. Since the difference in total reflectance at 242 nm and at 250 nm was only 0.2% and since the ARC spins to 250 nm at 4000 rpm, then 4000 rpm was chosen as a convenient spinning speed.

The parameters for spinning ARC layer and the photoresist for this particular research are given in Table 3.2. After spinning, each liquid is heated on a hotplate in order to evaporate the solvent.

After exposure the photoresist is cured at 110°C for 90 seconds, then developed using tetramethyl ammonium hydroxide commercial photoresist developer (CD-26®) by Shipley Company, Inc. Development is the process step that creates the physical holes in the photoresist layer. The PS-4 photoresist development takes a maximum of 60 seconds at

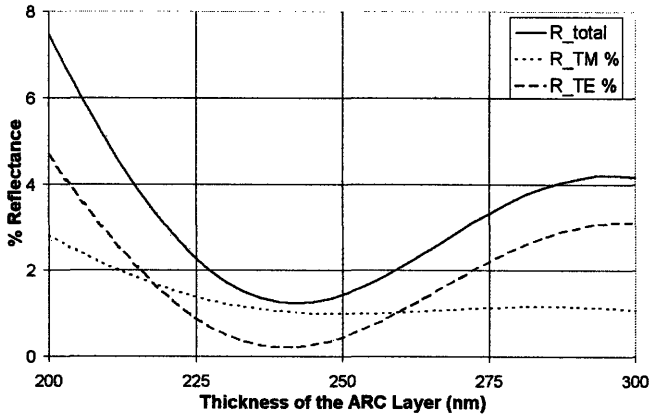

Figure 3.14: Percent of reflected power for transverse electric (TE) and transverse magnetic (TM) waves as a function of the thickness of the anti-reflective coating (ARC) layer. Notice that minima exist for TE and TM reflection around 240 nm of ARC thickness.

Table 3.1: Parameters for the reflectance simulation

Material	Real Index	Imaginary Index	Permeability	Thickness (m)
Air	1	0	1	1
Photoresist	1.681	-0.016	1	210e-9
ARC	1.55	-0.14	1	200-300e-9
Chromium	1.12	-2.95	1	50e-9
Tungsten	2.99	-2.56	1	1

room temperature. The sample is dried using gaseous nitrogen. The resulting structure is shown in Fig. 3.15.

3.2.1 Hexagonal Pattern Lithography

Lloyd's mirror capabilities for hexagonal patterning were also explored as they may be of interest in future pattern fabrication. A square pattern of holes leaves a large area of flat

Table 3.2: Parameters for ARC and photoresist spinning and baking

Material	Desired Thickness	rpm	Bake Temperature	Bake Time
ARC	250 nm	4000	175°C	90 seconds
Photoresist	210 nm	3000	90°C	90 seconds

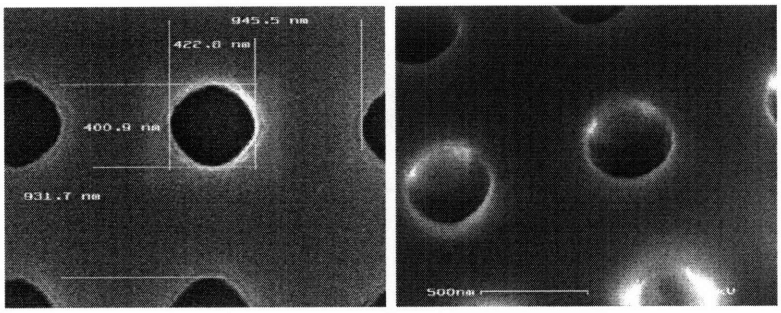

Figure 3.15: SEM images of top (left) and edge (right) views of the developed sample pattern after a double (2D) 80-second exposure at 0.25 μW and a one-minute PR development in CD-26 developer

tungsten between the holes, whereas a hexagonal pattern would minimize the flat tungsten surface area between holes. Depending on the final application, minimized surface between holes may be desirable. Figure 3.16-a illustrates the case of triple-exposure with perfect 60^o offsets. Figure 3.16-b illustrates the case in which the exposures angles are are not exactly 60^o.

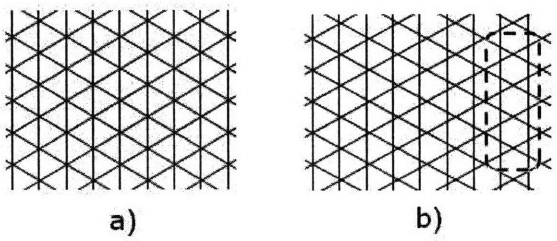

Figure 3.16: Triple exposure: a) with exact offset angle control - notice uniformity of intersections throughout the whole exposure area; b) with slightly different offset angles between exposures - notice that the three exposures do not intersect uniformly.

Figure 3.17 shows an SEM image of a triple-exposure (45 seconds each at 0.25 μW outlet power using a laser emitting at 325 nm) carried out in the NSL using the laser interference lithography system (silicon substrate). In the area in which the three exposures intersect perfectly, a triangular pattern of round holes is formed. The exposure system that is available in the NSL is not capable of precise control of rotation angles between exposures, so the areas of perfect intersections are limited. The angle between exposures is set manually, and no angle calibration is available. However, the laser interference lithography system can be modified to include precise control of the angles between the exposures. Precise angle control can be accomplished using an angle-variable stage for the sample holder. The radius of the hole, as in the square pattern case, can be controlled by adjusting the exposure time.

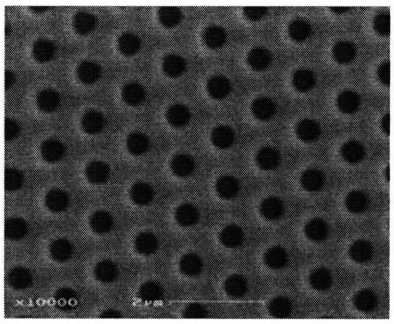

Figure 3.17: Triple exposure laser interference lithography SEM: a hexagonal pattern of round holes is formed in photoresist wherever the three exposure directions intersect properly.

This experiment demonstrated the capability for producing hexagonal patterns should such be needed. Lack of precise angle control between exposures makes the current lithography technique a bit impractical for large-scale exposures. However, with the addition of precise angle control this system could produce hexagonal patterns just as easily as rectangular arrays of holes.

3.3 Etching

After the lithography process the structure consists of a patterned layer of photoresist and the un-patterned underlying layers of ARC and the chromium hard-mask. The chromium hard-mask layer is necessary because the photoresist/ARC double-layer is not resistant to the tungsten etch chemistry. In the etching phase of the microfabrication process, there are three etch steps and they are described below.

3.3.1 Anti-Reflective Coating Reactive Ion Etching

Oxygen-based reactive ion etching (RIE) is used to transfer the pattern from the photoresist into the ARC layer. The RIE apparatus used for etching is a Plasma-Therm 790 Series RIE System.

Ion etching is a low-pressure dry gas etching technique that is widely used in microfabrication. RIE refers to highly-directional plasma etching. The gas with which the etching is performed is chosen based on the material being etched. The reaction product between the etched material and the etching gas is a volatile compound. The mask material is chosen such that it has a relatively slow reaction rate with the etching gas.

The outcome of the ARC RIE process determines the starting point for the next step. Therefore, it is very important to preserve a small round holes at the end of the ARC RIE process. A series of ARC RIE experiments were conducted to determine the minimum time required to transfer the pattern from the photoresist layer into the ARC layer without widening the hole.

The parameters for this step are a 2:1 (10 sccm : 5 sccm) mixture of helium and oxygen, with 7 mTorr pressure and 250 V bias. The etch rate is highly dependent on the power achieved during the etch process. While power primarily depends on the voltage, it also depends on the state of the etching chamber. Residual impurities from previous etches can easily influence the power by as much as 10%. A batch of calibration tests should always be conducted to take into account the current physical condition of the chamber.

Figure 3.18 shows the results of ARC RIE etch experiments with times varying from 4 minutes and 30 seconds down to 3 minutes. The shortest experiment, lasting three minutes, resulted in residual ARC in the holes (Fig. 3.18-d). Therefore, the optimum ARC RIE time is 3 minutes and 30 seconds, which allows for complete pattern transfer into the ARC layer without substantially widening the holes. The result of a 3.5-minute ARC etch on our prototype 1 sample is shown in Fig. 3.19.

3.3.2 Chromium Hard-Mask Wet Etch

In the chromium wet etch process, the pattern is transferred from the ARC layer into the chromium hard-mask layer by wet chemical etching. The chromium etchant used is Cyantek CR-7®, a commercially available chromium etchant manufactured by the Cyantek Corporation. The CR-7 etchant is diluted with 40% distilled water. The dilution assures repeatability of results by slowing down the etch rate and allowing appropriate reaction time when the desired diameter of the hole is reached.

Initially, undiluted CR-7 etch was used. Figure 3.20 shows sample SEMs before and after a one-minute CR-7 etch. The CR-7 etchant takes 30-40 seconds to attack the chromium surface and start etching. Once the etching starts, it proceeds rapidly at varying rates. Calibration experiments have shown etch rates as high as 10 nm/sec. Such high and unpredictable etch rate makes it very difficult to time the proper duration of the etch for the desired hole diameter. The control of the hole diameter is greatly improved by using diluted CR-7 etchant.

The chromium etch was the most unreliable in the first prototype fabrication. Etch rate non-linearity made it very difficult to control the diameter of the holes and extremely difficult to obtain repeatable results. To address this issue, a modified chromium etch process was developed. CR-7 etchant is a water-based solution. The etch rate is dependent on the proportion of acids in the water solution. For the second and third prototype a mixture of

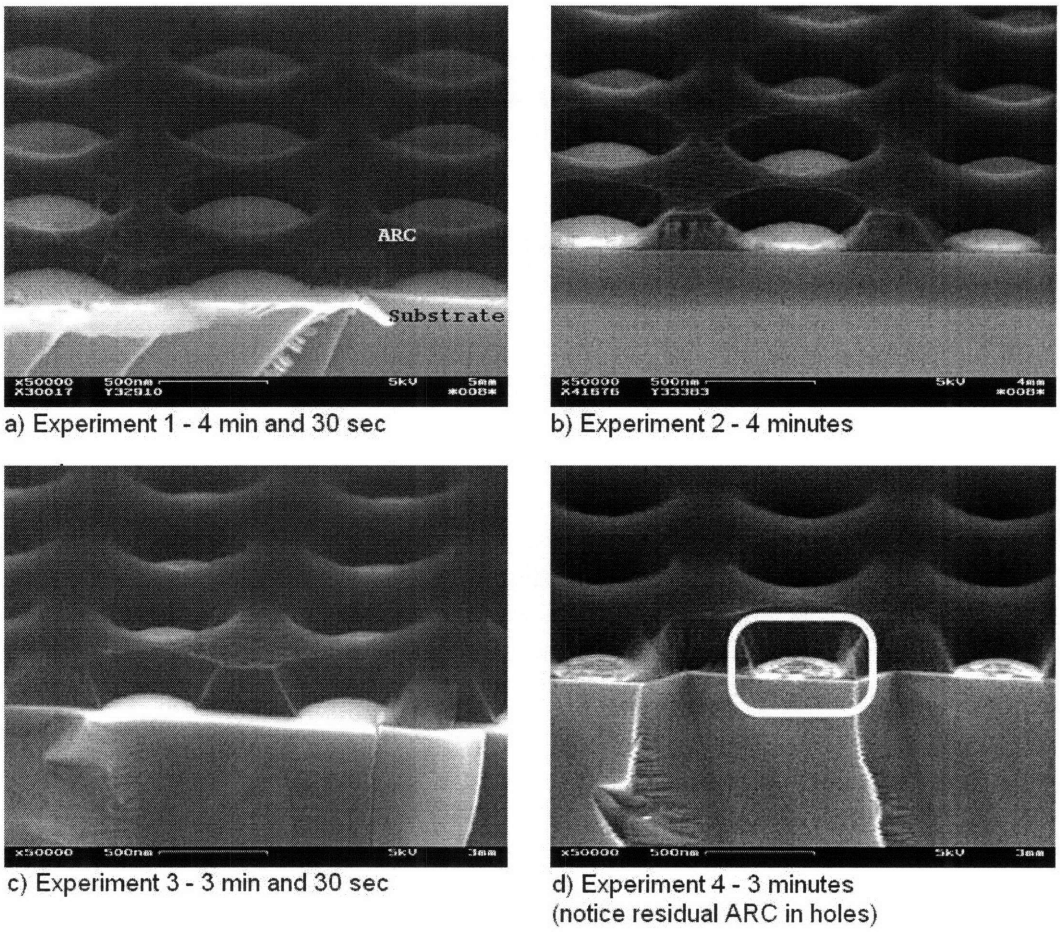

Figure 3.18: ARC RIE calibration experiments at 140-145 W RF power and 240-245 V DC bias

60% CR-7 and 40% distilled water was used. The dilution resulted in a linear relationship between the etch time and hole diameter (Fig. 3.21).

Upon completion of the chromium etch step, the sample is rinsed in distilled water and dried using gaseous nitrogen. The remaining ARC layer was removed using the same RIE recipe as was used to transfer the pattern from the photoresist into the ARC layer. Complete removal of the ARC layer was achieved after 5 minutes at 140 W.

Recall that in Sec. 3.1 a note was made regarding the influence of the chromium layer quality on pattern precision. Figure 3.22 illustrates the difference in CR-7 etch results due to the quality of the chromium layer. In the sample on the right, the chromium layer was deposited in a freshly-cleaned e-beam chamber. The improvement in wall smoothness is easily observed.

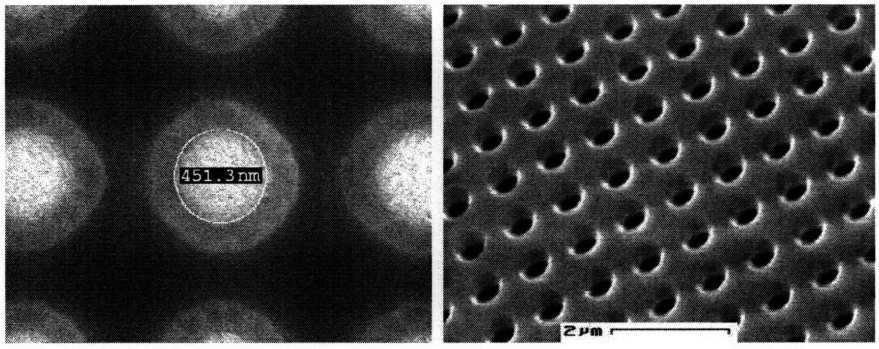

Figure 3.19: SEM images of top (left) and edge (right) views of ARC on top of chromium hard mask, after the ARC etch in He/O_2 for 3 minutes and 30 seconds

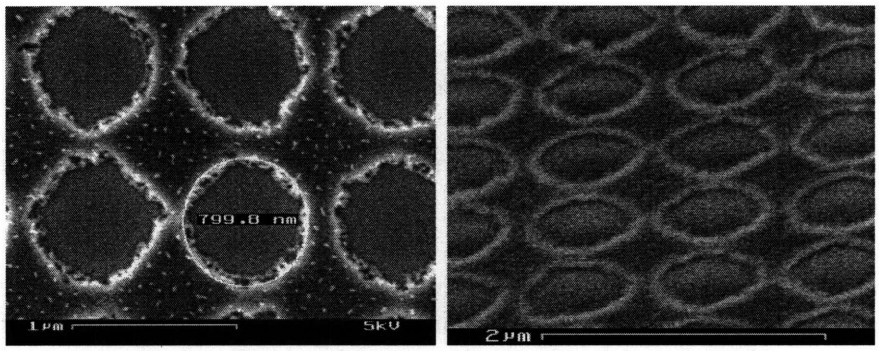

Figure 3.20: SEM images of etched chromium hard-mask on top of tungsten substrate (prototype 1): top (left) and edge (right). Chromium hard-mask was removed during a one-minute etch in Cyantek CR-7. The ARC layer was removed using He/O_2 RIE.

3.3.3 Tungsten Reactive Ion Etching

In the final etch step, carbon-tetrafluoride-based RIE is used to transfer the pattern from the chromium hard-mask layer into the tungsten substrate. The depth to which tungsten can be etched is determined by two direct parameters: the etch rate and the thickness of the chromium mask. Through the etch rate parameter, the achievable depth also depends on the gases, pressure, and power used in the RIE process.

Three tests were conducted to determine if the duration of the tungsten etch affects the etch rate. It was observed that for etches longer than 5 minutes, the etch rate saturates. Therefore, incremental etch steps of 5 minutes were used. Figure 3.23 illustrates the results of tungsten etch tests for 3, 5, and 7 minutes. Notice that the 7-minute etch (42 nm of depth) does not deliver an increase over the depth achieved during the 5-minute etch (52 nm of depth).

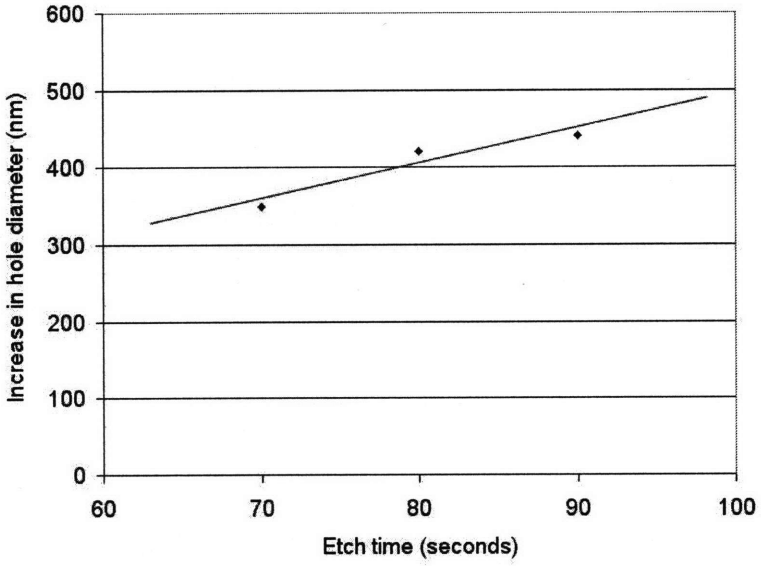

Figure 3.21: Diluted CR-7 etch with experimental points and trendline. Chromium thickness was held constant at 50nm.

The chromium mask thickness is slowly reduced during the tungsten RIE process. Experimental results show that for every 10 nm of tungsten, approximately 1 nm of chromium is sputtered away. However, this relationship is not linear. The chromium mask is initially very durable, but erodes with prolonged exposure to the tungsten RIE. Experiments conducted during this research show that the thickness (Th) of the chromium layer follows the trend of:

$$Th = C_1 - C_2 e^{tC_3} \tag{3.2}$$

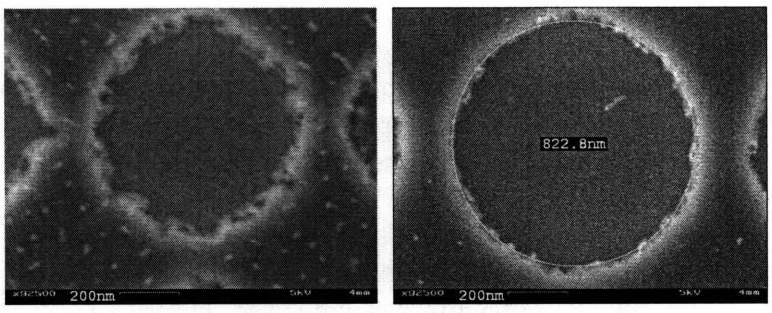

Figure 3.22: Comparison of CR-7 wet etch results for chromium layers deposited in uncleaned, high-pressure deposition chamber conditions (left) and cleaned, low-pressure deposition chamber conditions (right)

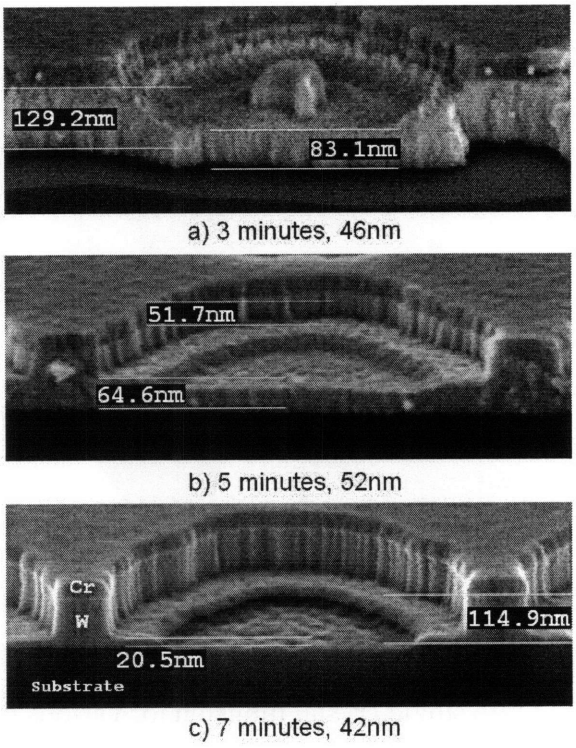

Figure 3.23: Initial tests of tungsten RIE with varying durations

where t is time, and C_1 (initial thickness of the chromium layer), C_2, C_3 are constants particular to the equipment and parameters used in the process. Typical values for C_2 and C_3 (for the equipment and materials used in this research) fell into the 0.45-0.55 and 0.04-0.09 ranges, respectively. To preserve top-surface quality the tungsten RIE process must stop before the chromium layer completely etches away. In our particular case, 50 nm of chromium will last until approximately 600 nm of depth is etched in tungsten.

Achievable depth of the tungsten features also depends on the power, pressure, and the proportion of gases used in the process. A new battery of tests was conducted to determine the influence of pressure and power on the etch rate and the damage to the chromium mask. The summary of differences between the various tests is outlined in Table 3.3.

Figures 3.24 and 3.25 illustrate the differences in achieved etch depth and percentage of remaining chromium mask for these tests. The maximum depth was achieved for Test 3. However, Test 3 also had the most severe damage to the chromium mask.

These tests offered insight into the influence of power and pressure on the etch rate and chromium mask destruction. Relative comparison of these tests indicates that Test 1 parameters are optimal for achieving a balance between etch rate and mask damage.

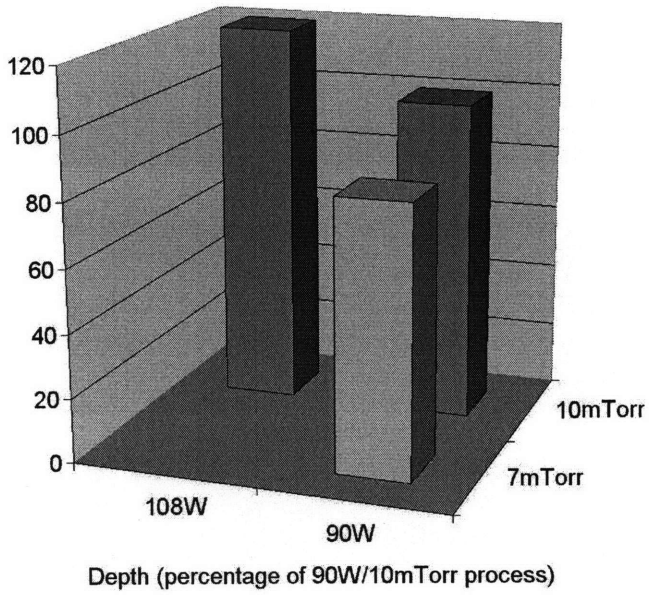

Figure 3.24: Depth etched into single-crystal tungsten for various tungsten RIE power and pressure

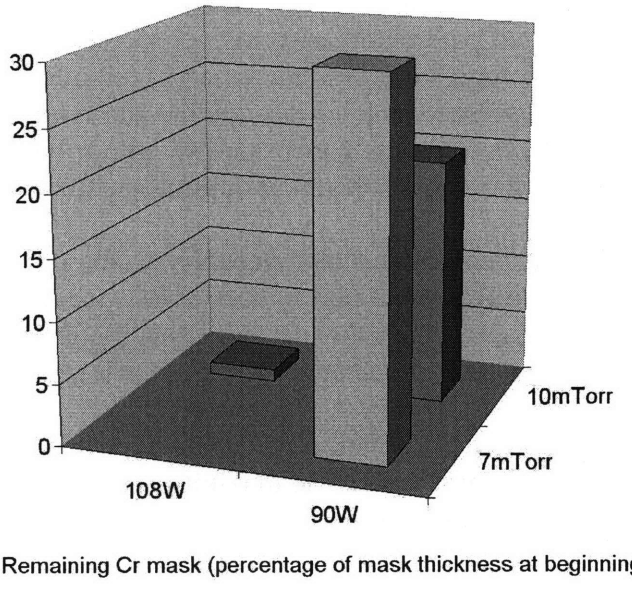

Figure 3.25: Remaining chromium mask thickness in single-crystal tungsten RIE experiments with varying power and pressure

Table 3.3: Tungsten RIE test results for various power and pressure combinations

	Test 1	**Test 2**	**Test 3**
Power	90 W	90 W	108 W
Pressure	10 mTorr	7 mTorr	10 mTorr
Etch depth	100%	84%	120%
Remaining Chromium	20%	30%	0%
Advantages	Little mask damage	Little mask damage	High etch rate
Disadvantages	Medium etch rate	Low etch rate	Mask damage

The prototype 1 time-lapse results (taken every 15 minutes) of the tungsten RIE process ($CF_4 : O_2 = 6.7 : 1$, 10 mTorr, 80 W) are shown in Fig. 3.26. Similar time-lapse SEM images for prototype 3 are shown in Fig. 3.27. Significant improvement in wall verticality and smoothness can be observed.

Although prototype 3 has much smoother sidewalls than prototype 1, some roughness is still present. The rough vertical lines in tungsten originate in the chromium wet etch process. The roughness of the chromium mask is transferred into the tungsten layer during the RIE process. The RIE process transfers and accentuates these irregular shapes. The rough features in the tungsten walls are on average about 20 nm in size, and the largest features at most 50 nm in size. These dimensions are orders of magnitude smaller than our radiation wavelength range (few micrometers), and therefore are expected to have little influence on the overall spectrum shape and selective emitter efficiency.

3.4 Summary

This chapter presented the flow of the fabrication process and the crucial parameters of each step. Although single-crystal tungsten processing is highly uncommon in today's semiconductor industry, we were able to develop a relatively simple, fast, and fab-friendly process. Should this process reach industry, batch and pipeline processing can be implemented enabling large-scale industrial production.

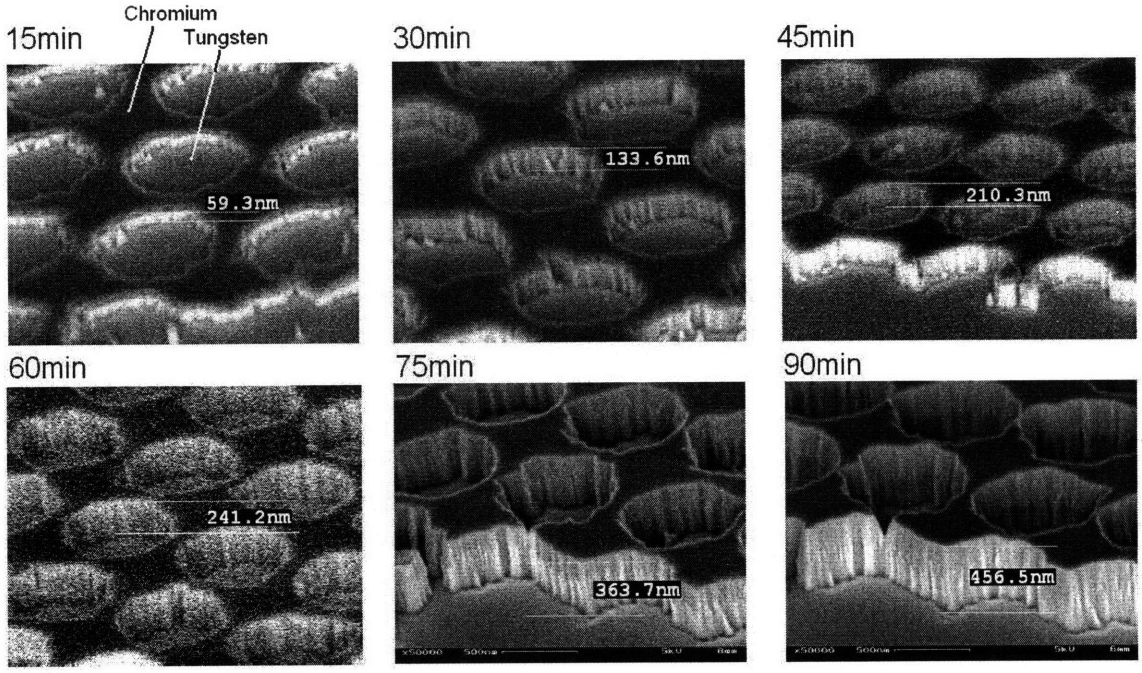

Figure 3.26: SEM images of prototype 1 tungsten RIE progress over time (edge views at 60°)

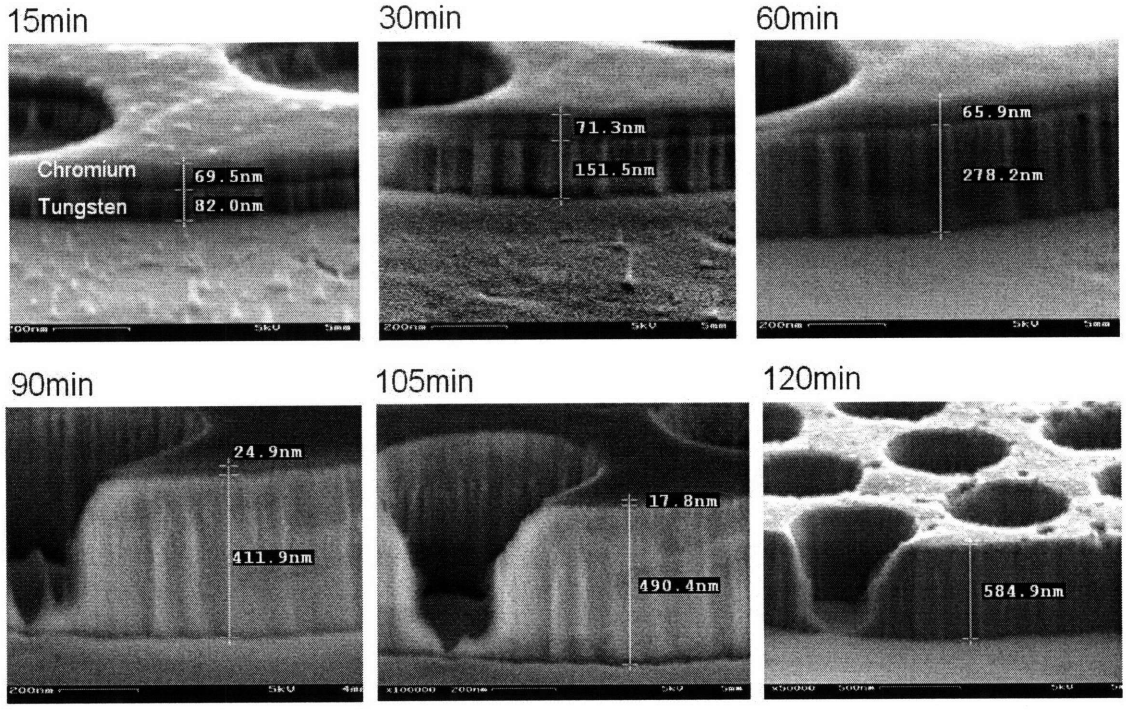

Figure 3.27: SEM images of prototype 3 tungsten RIE progress over time (edge views at 75°)

Chapter 4

Summary

This chapter encapsulates the material presented in this thesis. A summary of accomplishments is put forward, and recommendations for future research are offered.

4.1 Summary of Accomplishments

Chapter 1 introduced TPV energy conversion systems and their basic components. TPV history was reviewed, emphasizing the role of spectral control in the quest for high-efficiency TPV systems. Several possible paths of efficient spectral control are considered, and the motivation behind focusing on selective emitters is presented. It is concluded that PhC-based tungsten selective emitters have the potential to radically improve TPV system efficiency.

Chapter 2 presented a detailed investigation of three broad-band selective emitter prototypes. Theory is briefly reviewed, focusing on the dominant cavity and planar-surface effects. The dimensions of the prototypes were in accord with design specifications. Room-temperature optical properties were found to be in agreement with simulations, and spectral efficiencies in excess of 93% were measured. High-temperature radiative properties indicate a three-fold improvement over flat tungsten, and confirm our spectral performance expectations. An alternative prototype substrate, poly-crystalline tungsten foil, was investigated, and was found to have potential for substantial cost savings in the selective emitter production. Overall, our selective emitter designs are a great advance towards increasing spectral efficiency.

Chapter 3 contains the fabrication process investigations, development, and rigorous characterization procedures. We have focused on dimensional reliability, precision, and repeatability of the processes, with large-scale industrial production in mind. For each fabrication step, both characterization and final parameters are included.

4.2 Recommendations for Future Investigations

This thesis has focused on fabrication and characterization of selective emitters for TPV systems. While some major contributions were made, there are a number of issues yet to be investigated before TPV systems are fully understood. Based on the knowledge acquired during the course of this research, the following future investigations are suggested:

1. alternative mask etching techniques to address wall smoothness and verticality, specifically investigating the applicability of dry-etching techniques on materials that are suitable as tungsten hard-masks
2. materials investigation of the reactive ion etch influence on the optical quality of tungsten
3. cost-efficient tungsten foil substrate preparation and characterization, focusing on meeting fabrication requirements in terms of substrate smoothness and flatness while maintaining the cost advantage over single-crystal tungsten wafers
4. methods of producing larger-scale tungsten substrates and abutting selective emitters to form the large, uniform surface needed for larger TPV systems
5. durability of materials and patterns at high temperatures, possibly expanding investigations to include ceramic or other types of coatings resistant to high-temperature stresses
6. minimum required atmospheric conditions for tungsten selective emitters, balancing the material sensitivity with any system complexity and cost increases due to the vacuum requirement, and
7. system integration issues, such as fuel choice and delivery, vacuum packaging, and thermal management for TPV systems.

Selective emitters based on 2D PhC have significant potential of increasing the overall TPV system efficiency, and consequently hastening the commercialization of TPV systems. Although the focus of this research is the application of 2D PhC to TPV systems, the possibility of their application to other fields remains open.

References

[1] R. E. Nelson, "TPV Systems and State-of-Art Development," *Proceedings 5th Conference on Thermophotovoltaic Generation of Electricity*, vol. 653, pp. 3, September 2002.

[2] P. Aigrain, "The Thermophotovoltaic Converter," unpublished lectures given at the Ecole Normale Superieure in 1956, and the Massachusetts Institute of Technology, Fall 1960 and Spring 1961.

[3] G. Guazzoni and S. Matthews, "A Retrospective of Four Decades of Military Interest in Thermophotovoltaics," *Proceedings 6th NREL Conference on Thermophotovoltaic Generation of Electricity*, vol. 738, pp. 3, June 2004.

[4] H. H. Kolm, "Solar-battery power source," *Quarterly Progress Report, Solid State Research, Group 35*, MIT-Lincoln Laboratory, Lexington, MA, pp. 13, May 1956.

[5] B. D. Wedlock, "Thermo-Photo-Voltaic Energy Conversion," *Proceedings IEEE*, vol. 51, pp. 694-698, May 1963

[6] David C. White, et al., "Recent Advance in Thermal Energy conversion," *Proceedings of the 15th Power Sources Conference*, pp. 125-132, May 1961.

[7] M. Planck, "Distribution of energy in the spectrum," *Annalen der Physik*, vol. 4, no. 3, pp. 553-563, 1901.

[8] L. Fraas, et al., "Electric Power Production Using New GaSb Photovoltaic Cells with Extended Infrared Response," *Proceedings 1st NREL Conference on Thermophotovoltaic Generation of Electricity*, 1994.

[9] M. Zenker and A. Heinzel, "Efficiency and Power Density Potential of a Combustion Driven Thermophotovoltaic System Using GaSb Photovoltaic Cells," *IEEE Transactions on Electron Devices*, vol. 48, no. 2, February 2001.

[10] F. O'Sullivan, "Fabrication and Testing of an Infrared Spectral Control Component for Thermophotovoltaic Power Conversion Applications," M.S. Thesis, Department of Electrical Engineering and Computer Science, MIT, June 2004.

[11] A. Licciulli, et al., "The Challenge of High-Performance Selective Emitters for Thermophotovoltaic Applications," *Semiconductor Science and Technology*, vol. 18, pp. S174, April 2003.

[12] E. Palik, *Handbook of Optical Constants of Solids*, Academic Press, 1985.

[13] G. H. Dieke, *Spectra and Energy Levels of Rare Earth Ions in Crystals*, Interscience, New York, 1968.

[14] R. E. Nelson, "Thermophotovoltaic Emitter Development," *Proceedings 1st NREL Conference on Thermophotovoltaic Generation of Electricity*, 1994.

[15] D. L. Chubb, "Reappraisal of Solid Selective Emitters," *Proceedings 21st IEEE Photovoltaic Specialists Conference*, 1990.

[16] R. A. Lowe, et al., "Radiative Performance of Rare Earth Garnet Thin Film Selective Emitters," *Proceedings 1st NREL Conference on Thermophotovoltaic Generation of Electricity*, 1994.

[17] I. Celanovic, et al., "1D and 2D Photonic Crystals for Thermophotovoltaic Applications," *Proceedings Photonics Europe 2004 Photonic Crystal Materials and Nanostructures*, International Society for Optical Engineering, vol. 5450, pp. 416, April 2004.

[18] H. Yugami, "Thermophotovoltaic generation with surface grating selective emitters based on tungsten single crystals," Invited Presentation to the MIT Department of Mechanical Engineering, September 29, 2004.

[19] E. Hecht, *Optics*, Addison-Wesley, Reading, MA, 1998.

[20] Lord Rayleigh, "On the Reflection of Light from a Regularly Stratified Medium," *Proceedings of the Royal Society of London*, vol. 93, no. 655, pp. 565-577, October 1917.

[21] K. M. Ho, C. T. Chan, C. M. Soukoulis, "Existence of a Photonic Gap in Periodic Dielectric Structures," *Phys. Rev. Lett.*, vol. 65, no. 25, December 1990.

[22] E. Yablonovitch, T. J. Gmitter, "Photonic Band Structure: The Face-Centered Cubic Case Employing Spherical Atoms," *Phys. Rev. Lett.*, vol. 67, no. 17, October 1991.

[23] S. Y. Lin, et al., "A three-dimensional photonic crystal operating at infrared wavelengths," *Nature*, vol. 394, July 1998.

[24] S. Y. Lin, et al., "Enhancement and suppression of thermal emission by a three-dimensional photonic crystal," *Phys. Rev. B*, vol. 62, no. 4, July 2000.

[25] J. Gee, et al., "Selective Emitters Using Photonic Crystals for Thermophotovoltaic Energy Conversion," *Proceedings IEEE Photovoltaic Specialists Conference 2002*, pp. 896-899, May 2002.

[26] A. A. Parker, et al., "Aphrodite's Iridescence," *Nature Magazine*, vol. 409, pp. 36, January 2001.

[27] B. S. Thornton, "Limit of the moth's eye principle and other impedance-matching corrugations for solar-absorber design," *J. Opt. Soc. Am.*, vol. 65, no. 3, march 1975.

[28] D. L. Chubb, et al. "A Small Particle Selective Emitter for Thermophotovoltaic Energy Conversion," *Proceedings of 2nd NREL Conference on Thermophotovoltaic Generation of Electricity*, 1995.

[29] W. E. Horne, et al., "Integrated Bandpass Filter Contacts for Radioisotope Thermophotovoltaic Cells," *Proceedings 31st International Energy Conversion Engineering Conference*, 1996.

[30] *Thermophotovoltaic Generator with Hermetically Sealed Emitter Thermos*, JX Crystals DARPA Final Report, 2001.

[31] H. Sai, et al., "Spectral Control of Thermal Emission by Periodic Microstructured Surfaces in the Near-Infrared Region," *Journal of Optical Society of America*, vol. 18, no. 7, July 2001.

[32] S. Maruyama, et al., "Thermal Radiation from Two-Dimensionally Confined Modes in Microcavities," *Applied Physics Letters*, vol. 79, no. 9, August 2001.

[33] H. Sai, et al. "Spectrally Selective Emitters with Deep Rectangular Cavities Fabricated with Fast Atom Beam Etching," *Proceedings of 5th NREL Conference on Thermophotovoltaic Generation of Electricity*, 2002.

[34] C. Schlemmer, et al. "Thermal Stability of Micro-Structured Selective Tungsten Emitters," *Proceedings of 5th NREL Conference on Thermophotovoltaic Generation of Electricity*, 2002.

[35] M. U. Pralle, et al. "Photonic Crystal Enhanced Narrow-Band Infrared Emitters," *Appl. Phys. Lett.*, vol. 81, no. 25, pp. 4685, December 2002.

[36] B. Wernsman, et al., "Greater Than 20% Radiant Heat Conversion Efficiency of a Thermophotovoltaic Radiator/Module System Using Reflective Spectral Control," *IEEE Trans. Elec. Dev.*, vol. 51, no. 3, pp 512, March 2004.

[37] P. M. Fourspring, et al. "Thermophotovoltaic Spectral Control," *Proceedings of 6th NREL Conference on Thermophotovoltaic Generation of Electricity*, 2004.

[38] I. Celanovic, "Thermophotovoltaics: Shaping the Flow of Thermal Radiation," Ph.D. Thesis, Department of Electrical Engineering and Computer Science, MIT, May 2006.

[39] D. Chan, et al., "Thermal Emission and Design in 2D-Periodic Metallic Photonic Crystal Slabs," *Optics Express*, vol. 14, no. 19, August 2006.

[40] D. E. Aspnes, "Local-field effects and effective-medium theory: A microscopic perspective," *Am. J. Phys*, vol. 50, no. 8, August 1982.

[41] *Ansoft High Frequency Structure Simulator Manual.* Pittsburgh, PA, USA: Ansoft Corporation, 2001.

[42] *Alldyne Technologies Product Catalogue 2007.* Huntsville, AL, USA: ATI Alldyne Allegheny Techologies Company, 2007.

[43] N. Jovanovic, et al., "Photonic Crystals for Thermophotovoltaic Applications," *MIT/Industry Consortium on Advanced Automotive Electrical/Electronic Components and Systems*, Semi-Annual Meeting, Cambridge, MA, October 26, 2005.

[44] B.T. Barnes, "Optical Constants of Incandescent Refractory Metals," *J. Opt. Soc. Am.*, vol. 56, no. 11, November 1966.

[45] M. Walsh, "Nanostructuring Magnetic Thin Films Using Interference Lithography," M.S. Thesis, Department of Electrical Engineering and Computer Science, MIT, August 2000.

[46] S. Tolansky, *Introduction to Interferometry*, Longmans, Green & Co., New York, 1955.

[47] H. Smith, *Submicron- and Nanometer-Structures Technology*, NanoStructures Press, Sudbury, MA, 1994.